ciRS-7-miR7 regulate ischemia induced neuronal death via glutamatergic signaling

Flavia Scoyni[1], Valeriia Sitnikova[1*], Luca Giudice[1*], Paula Korhonen[1], Davide M Trevisan[2], Ana Hernandez de Sande[3], Mireia Gomez-Budia[1], Raisa Giniatullina[1], Irene F Ugidos[1], Hiramani Dhungana[4], Cristiana Pistono[1], Nea Korvenlaita[1], Nelli-Noora Välimäki[1], Salla M Kangas[5], Anniina E Hiltunen[6], Minna U Kaikkonen-Määttä[1], Jari Koistinaho[1,4], Seppo Ylä-Herttuala[1], Reetta Hinttala[5,6], Morten T Venø[7,8], Junyi Su[8], Markus Stoffel[9], Anne Schaefer[10,11], Nikolaus Rajewsky[12], Jørgen Kjems[8], Mary P LaPierre[9], Monika Piwecka[13], Jukka Jolkkonen[1], Rashid Giniatullin[1], Thomas B Hansen[8,14], Malm Tarja[1]

Affiliations:

[1]A.I.Virtanen Institute for Molecular Sciences, University of Eastern Finland, Kuopio, Finland
[2]Department of Biosciences and Nutrition, Karolinska Institute, Stockholm, Sweden
[3]School of Medicine, University of Eastern Finland, Kuopio, Finland
[4]Neuroscience Center, University of Helsinki, Finland
[5]Biocenter Oulu, University of Oulu, Oulu, Finland
[6]Medical Research Center Oulu and Research Unit of Clinical Medicine, University of Oulu and Oulu University Hospital, Oulu, Finland
[7]Omiics ApS, Aarhus, Denmark
[8]Interdisciplinary Nanoscience Center, Department of Molecular Biology and Genetics, Aarhus University, Aarhus, Denmark
[9]Institute of Molecular Health Sciences, ETH Zurich, Zürich, Switzerland
[10]Departments of Neuroscience and Psychiatry, Icahn School of Medicine at Mount Sinai, New York, USA
[11]Max Planck Institute, Biology of Ageing, Cologne, Germany
[12]Systems Biology of Gene Regulatory Elements, Max-Delbrück-Center for Molecular Medicine in the Helmholtz Association (MDC), Berlin Institute for Medical Systems Biology (BIMSB), Berlin, Germany
[13]Institute of Bioorganic Chemistry, Polish Academy of Sciences, Poznan, Poland
[14]Present address: Targovax ASA, Lysaker, Norway

*These authors contributed equally to this work

ABSTRACT

Brain functionality resides on finely tuned regulation of gene expression by networks of non-coding RNAs (ncRNAs) such as the one composed by the circular RNA ciRS-7, the microRNA miR-7 and the long non-coding RNA Cyrano. However, very little is known on how this network regulates stress responses in neurodegeneration. Here we describe ischemia induced alterations in the ncRNA network both *in vitro* and *in vivo* and in transgenic mice lacking ciRS-7 or miR-7. Our data show that cortical neurons downregulate ciRS-7 and Cyrano and upregulate miR-7 expression upon ischemic insults. Mice lacking ciRS-7 show reduced lesion size and motor impairment, whilst the absence of miR-7 alone leads to an increase in the ischemia induced neuronal death. Moreover, miR-7 levels in pyramidal excitatory neurons regulate dendrite morphology and glutamatergic signaling suggesting a potential molecular link to the *in vivo* phenotype. Our data reveal a new endogenous mechanism by which ciRS-7 and miR-7 regulate the outcome of ischemic stroke and shed new light into the pathophysiological roles of intracellular networks of non-coding RNAs in the brain.

30 **INTRODUCTION**

31 The specialized, dynamic, and complex functionality of the brain relies on accurate regulation of gene
32 expression, also mediated by non-coding RNAs (ncRNAs) which are particularly overrepresented in
33 the brain and have been strongly connected with the increase of cognitive complexity in human[1].
34 MicroRNAs (miRNAs) are short (~22 nucleotides) ncRNAs known to post-transcriptionally regulate
35 the expression of messenger RNA (mRNA) by binding short complementary sequences (seed)[2] and
36 triggering mRNA decay or inhibition of translation[3]. Long non-coding RNAs (lncRNAs) are
37 molecules of regulatory RNA longer than 200 nucleotides capable of regulating gene expression by
38 interacting with other ncRNAs such as miRNAs, or proteins through secondary structures[4]. Circular
39 RNAs (circRNAs) belong to a novel class of ncRNAs that, among other functions, are able to
40 modulate gene expression by interacting with miRNAs, hence affecting miRNAs activity on mRNA
41 targets[5]. CircRNAs are generated by backsplicing of linear transcripts, a specific splicing event in
42 which the 5' splice site of the upstream exon binds to the 3' splice site of the downstream exon[6].
43 Thus, in RNA-sequencing data, the reads on the backsplice junction identify the circular specific form
44 of the transcript and the circRNA abundance is defined by the ratio of these reads to the canonical
45 splicing reads.

46

47 These ncRNAs independently control cellular function by regulating the expression of protein coding
48 genes, but also interact with each other. An excellent example of ncRNAs regulatory network is the
49 brain specific network composed by two miRNAs (miR-7, miR-671), a lncRNA (Cyrano) and a
50 circRNA (ciRS-7)[5,7–9]. ciRS-7 is suggested to stabilize and promote miR-7 targeting through
51 delocalization of miR-7 in different neuronal compartments[8,9]. On the other end, Cyrano has a single
52 site of almost perfect complementarity to miR-7 which induces the degradation of miR-7 through
53 target RNA–directed miRNA degradation (TDMD)[8]. The regulation of miR-7 mediated by Cyrano
54 affect ciRS-7 abundancy and localization creating a network of interactions between these molecules
55 that at the same time indirectly affect the expression of miR-7 target genes[5,8–10]. Gain and loss of

56 function experiments and the development of knock-out animals for ciRS-7, miR-7 and Cyrano have
57 revealed that Cyrano and ciRS-7 bind miR-7 and regulate its expression[5,8,9]. Nonetheless, no
58 information is available on how this network regulates gene expression in pathophysiological
59 conditions.
60
61 Ischemic stroke, induced by occlusion of one of the main cerebral arteries, leads to lack of oxygen
62 and nutrients in the brain parenchyma and subsequent cell death. Lack of energy and disruption in
63 the ion balance cause an uncontrolled release of glutamate in excitatory neurons and deficient uptake
64 of glutamate by astrocytes induces glutamate excitotoxity[11] and subsequent oxidative stress, necrosis
65 and apoptosis[12]. Due to the complexity of the ischemic stroke pathophysiology, it is not surprising
66 that numerous miRNAs and lncRNAs have been identified to regulate oxidative stress response and
67 glutamate excitotoxicity contributing to the outcome of stroke[13]. In fact, when the stress is sustained,
68 miRNAs are known to be involved in adaptative sudden switches of gene expression programs[14]. The
69 efficiency of miRNA-mediated target repression depends on the availability of miRNAs to interact
70 (expression, localization, activity) and the amount of mRNA targets that have a seed Mirna
71 Recognition Element (MRE), which confer robustness to crucial cellular functions creating a miRNA-
72 specific threshold[15]. In this context, sudden changes in MRE containing sequences can lead to an
73 imbalance in miRNA targeting and de-repression of specific targets. The crosstalk between miRNA
74 and all the expressed sequences containing MRE at any given moment suggested a theory that in
75 physiological conditions, a large number of MRE sequences compete for the binding of the miRNA[16].
76 Moreover, the expression of specific transcript with different binding strength or MRE abundance
77 during stress is known to be used by organisms to regulate miRNA effects in a process called target
78 mimicry[17].
79

80 Recent studies have also highlighted a strong connection between circRNAs and the production of
81 reactive oxygen species[18]. However, even though single ncRNAs have been studied in the context of
82 ischemic stroke[13], a comprehensive analysis of the regulatory role of ncRNAs network in stroke is
83 still lacking. In this study, we identified the brain highly expressed circRNA, ciRS-7, as one of the
84 seven circRNAs deregulated in ischemia-related conditions *in vitro* and *in vivo*. We expanded our
85 analysis to other ncRNAs species and discovered additional changes in miR-7 and Cyrano which
86 belong to the same regulatory circuitry of ciRS-7. Using ciRS-7 and miR-7 knock-out mouse models,
87 we revealed the potential role of ciRS-7 in preventing miR-7-mediated regulation of the target
88 mRNAs and demonstrate that ciRS-7 molecular network is involved in the regulation of stroke-
89 induced cell death.
90
91
92 **RESULTS**
93
94 ***Oxygen and glucose deprivation induces changes in the expression of circular RNAs***
95 As circRNAs were previously connected to oxidative stress response[18] we evaluated the potential
96 deregulation of circRNAs in conditions mimicking ischemic stroke *in vitro*. We cultured murine
97 cortical neurons isolated from embryonic day fifteen (E15) cortices, subjected them to oxygen and
98 glucose deprivation (OGD) (Supplementary Figure S1A) and performed total RNA sequencing. To
99 assess whether our neuronal culture is composed of cell types representative of the murine cortex,
100 we inferred the presence of individual cell populations in our bulk RNA-seq samples through a
101 deconvolution analysis on single-cell RNA-seq dataset of embryonic mouse brain (E14.5[19]). The
102 results confirmed that interneurons (Int) and pyramidal neurons (Layer V-VI) are the most abundant
103 cell populations in our culture (Figure 1A). To validate that the culture is effectively enriched in
104 functional Interneurons (*GABAergic*) and Pyramidal neurons (*Glutamatergic*), we stimulated our
105 neuronal culture with GABA and glutamate and recorded the consequent induction of intracellular
106 calcium using calcium imaging. Our data confirmed that 98% of cells in our culture responded to

107 glutamate and 36% to GABA, providing functional proof that our culture mostly consists of
108 glutamatergic excitatory neurons (Figure 1B).
109 Ingenuity Pathway Analysis (IPA) of the differentially expressed transcripts between normoxic and
110 OGD neurons confirmed that OGD treatment induced the activation of Hypoxia-inducible factor 1-
111 alpha (HIF-1alpha) (Figure 1C) and downstream upregulation of glycolysis, a characteristic hallmark
112 of OGD[20] (Supplementary Table S1). Moreover, colorimetric cell viability assay indicated 30%
113 decrease in neuronal viability upon the exposure (Supplementary Figure S1B), validating that our
114 experimental setting represents a population of glutamatergic excitatory neurons that are vulnerable
115 to ischemia-induced cell death.
116 CircRNAs are generated by back-splicing which produces transcripts that can be detected with back-
117 splice junction reads (BSJ) spanning regions that are not present in regularly spliced transcripts
118 (forward splice junction reads, FSJ) (Figure 1D). In order to identify OGD-induced alterations in
119 circRNAs, we used *CIRIquant* algorithm[21], which considers circular specific reads (BSJ) and their
120 ratio with linear transcript reads (FSJ), and identified 27 circRNAs with high confidence of which 7
121 were significantly differentially expressed (DE) between normoxic (control) and OGD conditions
122 (Figure 1E, Supplementary Table S2). Among these DE circRNAs, ciRS-7 was the most highly
123 expressed yielding the highest number of back-splice junctions (Figure 1F, left) and the highest
124 circular to linear ratio (Junction ratio) (Figure 1F, right). In fact, ciRS-7 obtained a junction ratio
125 score above 0.8, meaning that more than 80% of the transcripts originating from this locus are
126 circular, in contrast with the other circRNAs which showed about 40% circular expression.
127 Specifically, ciRS-7 was one of the three downregulated circRNAs upon OGD.
128
129 ***ciRS-7 network is altered in conditions mimicking ischemic stroke in vitro***
130 ciRS-7 has been shown to be part of a feedback loop with miR-671 and miR-7 microRNA[5,7] and
131 indirectly, through miR-7, with the long non-coding RNA Cyrano[8] (Figure 2A). To investigate the

132 relative relationship between these players in *in vitro* OGD conditions, we performed small RNA
133 sequencing of cortical neurons exposed to OGD. Together with the previously presented dataset, we
134 were able to capture circRNAs, mRNAs, long non-coding RNAs and small RNA transcripts
135 (Supplementary Table S2).
136 Small RNA-sequencing identified 333 upregulated and 88 downregulated miRNAs following OGD
137 (Figure 2B). The levels of miR-671-5p remained unaltered (Figure 2B) which was confirmed
138 independently by RT-qPCR (Supplementary Figure S2A), in contrast to previous findings of
139 diverging miR-671-5p and ciRS-7 expression in different contexts[7–9]. Instead, we detected a
140 significant upregulation in miR-7a-5p, but not of the variant miR-7b-5p (Figure 2B, Supplementary
141 Table S2). Similarly to human, in mouse miR-7 is redundantly encoded by three different loci (*miR-*
142 *7a-1*, *miR-7a-2*, *miR-7b*), each is produced from different primary transcript (pri-miRNA) and
143 precursor (pre-miRNA). Further processing, in all cases from -5p arm, give rise to two mature miR-
144 7 sequences (miR-7a and miR-7b), differing only by a single nucleotide in the non-seed position
145 number 10 (Figure 2C). To study the expression of these three miR-7 loci in our system, we took
146 advantage of Global run-on sequencing (GRO-seq), which allows the capture of nuclear nascent RNA
147 primary molecules, and compared our murine culture expression[22] with different mouse tissues and
148 cell lines[22–32] (Supplementary Table S3). In physiological conditions, only cortical neurons and the
149 pituitary gland actively transcribe all three independently regulated *miR-7* loci (Figure 2D). The
150 active transcription from three different loci in neuronal cells suggests a higher order of regulation of
151 this miRNA which influences the mature forms. Under OGD conditions, only the pri-miRNAs
152 contributing to the expression of miR-7a (miR-7a-1 and miR-7a-2) were significantly upregulated
153 (Figure 2E), indicating that the observed upregulation occurs already at the level of transcription.
154 None of miR-7 passenger strands generated from the three precursors (miR-7a-1-3p, miR-7a-2-3p,
155 and miR-7b-3p) were altered in our sequencing data (Supplementary Table S2). Moreover, we
156 detected no changes in the host gene in which miR-7a-1 is embedded *(Hnrnpk*), and from which the

157 most abundant miR-7 primary transcript is generated (Supplementary Table S2). Taken together these
158 data show that OGD specifically regulates miR-7a-5p variant at the transcriptional and/or post-
159 transcriptional level.
160
161 To test the possible functional relevance of the upregulation of miR-7a-5p, we acquired predicted and
162 validated targets of miR-7a-5p using *miRWalk* algorithm analysis[33,34] and compared their overall
163 expression in conditions of OGD. In accordance with the upregulation of miR-7, miR-7 targets
164 showed a significant overall downregulation (Figure 2F, Supplementary Table S4), suggesting a
165 canonical functional repressive role of this miRNA.
166 The role of miR-7 interaction with ciRS-7 remains controversial, and it is thought to set the balance
167 between a positive and negative feedback[8,9] (Figure 2A). Additionally, Cyrano promotes template
168 mediated degradation (TMD) of miR-7 through a site of almost perfect complementarity, which was
169 shown to indirectly regulate ciRS-7 levels and localization[8] (Figure 2A). In our dataset the lncRNA
170 Cyrano was significantly downregulated upon OGD (Figure 2G), in line with the observed
171 upregulation in miR-7a-5p (Figure 2B).
172 To identify a first responder to OGD in the context of this molecular circuitry we evaluate the time-
173 dependent changes in the levels of these molecules. We subjected cortical neurons to OGD for 1, 6,
174 12 and 24 hours and assessed the expression level of ciRS-7, miR-7 and Cyrano. We detected a
175 significant downregulation of ciRS-7 and Cyrano already at 6 hours after OGD, prior to the
176 upregulation of miR-7 at 12 hours (Figure 2H). Interestingly, our data revealed a significant
177 downregulation of miR-7 at 6h of OGD concomitantly with downregulation in ciRS-7 and Cyrano,
178 which is in line with the previously suggested role of ciRS-7 in stabilizing miR-7[9].
179
180 ***ciRS-7 KO neurons exhibit differential OGD response***
181 The absence of ciRS-7 alters synaptic transmission in excitatory neurons and produces schizophrenia-
182 like phenotype *in vivo*[9], connecting this molecule to glutamatergic transmission. This is of particular

183 interest in conditions of ischemic stroke, where glutamate mediated excitotoxicity is a critical
184 contributor to neuronal cell death[12]. Our cortical neuron culture enriched in glutamatergic neurons
185 (Figure 1B) provides a system in which these events can be studied *in vitro.* Neurons cultured from
186 ciRS-7 KO mice showed higher Ca^{2+}-responses to the stimulation with glutamate compared to their
187 wild-type (WT) counterparts (Figure 3A). Consequently, ciRS-7 KO neurons also exhibited a
188 significantly higher sensitivity to excitotoxicity upon exposure to high concentration of glutamate
189 (Figure 3B).
190
191 To test if this increased sensitivity to glutamate is affecting gene expression changes in OGD, we
192 subjected the ciRS-7 KO cortical cultures to OGD following the previous experimental design
193 (Supplementary Figure S1A) and performed total RNA-seq. OGD induced deregulation in total of
194 5767 genes in ciRS-7 KO neurons compared to normoxic conditions, of which the 85% were shared
195 with WT neurons (Figure 3C). In response to OGD, 871 genes were differentially expressed only in
196 ciRS-7 KO neurons, while the expression 1260 genes was exclusively altered in WT neurons
197 subjected to OGD. ciRS-7 WT specific genes altered in OGD were functionally enriched in
198 mitochondrial processes, DNA metabolism, regulation of cell-cycle and oxidative stress-induced
199 apoptosis (Figure 3D). The 871 KO-specific genes were instead involved in developmental and pro-
200 regenerative processes (*progenitor migration to the cortex, DNA replication, transcription,*
201 *cerebellar cortex development*) (Figure 3E). Thus, even though the genetic predisposition to
202 glutamate sensitivity of ciRS-7 KO would suggest a deleterious outcome in the OGD response, ciRS-
203 7 KO neurons in OGD regulate pathways of resilience. In support of this, ciRS-7 KO neurons did not
204 show increased cell death compared to WT in response of OGD treatment (Supplementary Figure
205 S2B). Interestingly, the lack of ciRS-7 did not affect OGD induced changes in the expression of miR-
206 7 and Cyrano (Figure 3F). Similar to WT neurons, Cyrano lncRNA was downregulated in ciRS-7 KO
207 neurons responding to OGD (Figure 3F, Supplementary Table S5). Moreover, even though ciRS-7

208 KO neurons stably express lower levels of miR-7a-5p[9] (Figure 3F, Supplementary Table S5), small-
209 RNA sequencing revealed a significant upregulation of miR-7a-5p in response to OGD also in these
210 neurons (Figure 3F, Supplementary Table S5). In line with our previous findings, we detected no
211 changes in miR-671-5p, miR-7b-5p and miR-7 passenger strands expression (Supplementary Table
212 S5). Nonetheless, whilst the expression in miR-7a-5p in OGD remained lower in ciRS-7 KO neurons
213 compared to WT neurons (Figure 3F), the targets of miR-7a-5p, both predicted and validated, showed
214 a significant global repression in these conditions (Figure 3G).
215
216
217 ***Alteration of ciRS-7 network affects ischemic stroke outcome in vivo***
218 To evaluate the involvement of ciRS-7 network in ischemic stroke *in vivo*, *BALB/c* mice were
219 subjected to permanent middle cerebral artery occlusion (pMCAo) and levels of ciRS-7, Cyrano and
220 miR-7a-5p were evaluated by qPCR at six hours, one day and five days post-ischemia. In line with
221 our *in vitro* results, we detected a significant downregulation of ciRS-7 and Cyrano and upregulation
222 of miR-7a-5p in the peri-ischemic cortex (PI) at one day post-ischemia (dpi) compared to contralateral
223 cortex (CL) (Figure 4A). Moreover, similar to OGD, we failed to detect alterations in miR-671-5p
224 levels (Supplementary Figure S2C).
225
226 To evaluate the functional relevance of the ambiguous behavior of ciRS-7 KO neurons which showed
227 glutamate sensitivity but lack of increased cell death in OGD, we assessed whether ciRS-7 KO mice
228 subjected to transient ischemic stroke would show altered vulnerability to ischemic damage and
229 associated sensorimotor impairments. The size of the ischemic lesion was measured using Magnetic
230 Resonance Imaging (MRI) and behavioral deficits were assessed using Neurological Severity Scores
231 (NSS) at acute (1dpi), subacute (3dpi) and chronic (7dpi) timepoints after transient middle cerebral
232 artery occlusion (tMCAo) (Figure 4B). At 1dpi, ciRS-7 KO mice showed a significant reduction in
233 the ischemic lesion volume compared to their WT controls (Figure 4C) and significantly ameliorated

234 motor deficits (Figure 4D). Interestingly, ciRS-7 KO animals exhibited a reduced lesion size only
235 transiently at the acute timepoint (1dpi), showing no delay in the progression of the damage
236 (Supplementary Figure S3A,B).
237 To identify the molecular changes associated with the acute reduction in the lesion size and motor
238 deficits of the ciRS-7 KO mice, mice were sacrificed at 1dpi and peri-ischemic and the contralateral
239 cortex was used for mRNA sequencing. IPA analysis of the differentially expressed genes revealed
240 that ciRS-7 KO animals exhibited substantial inhibition in the pathways related to neuronal and tissue
241 damage, cytokine and interleukin release and calcium influx, in their peri-ischemic cortex compared
242 to WT controls (Figure 4E, Supplementary Table S6). Moreover, the differentially expressed genes
243 were mostly contributing to pathways of *necrosis* (205 genes) and *quantity of cytokine* (41 genes),
244 suggesting that the decreased lesion size in the ciRS-7 KO mice may be due to inhibition of necrotic
245 pathways and reduction in cytokine release.
246 In order to identify the major cellular responders mediating the observed alterations in gene
247 expression profiles, we carried out deconvolution analysis by using adult mouse brain scRNA-seq
248 data[35] to define the contribution of different cell populations to our bulk mRNA sequencing dataset.
249 This analysis identified neurons and astrocytes as major cellular responders contributing to the
250 differences between the WT and ciRS-7 KO gene expression profiles (Figure 4F). ciRS-7 KO mice
251 showed increased neuronal involvement in the peri-infarct cortex compared to the WT mice in line
252 with the significantly decreased tissue death in ciRS-7 KO mice, as measured by MRI (Figure 4C).
253 At the same time, ciRS-7 KO animals exhibited a decrease in the contribution of astrocytes in the
254 peri-ischemic cortex.
255 We then collected brain slices of ischemic ciRS-7 KO mice at 7dpi, timepoint of maximum immune
256 response[36], for staining with the astrocytic glial fibrillary acidic protein (GFAP). As expected,
257 ischemic stroke induced the expression of GFAP in the peri-infarct cortex in both WT and ciRS-7

258 KO mice. However, ciRS-7 KO mice showed significantly reduced astrogliosis in this area compered
259 to WT animals (Figure 4G).
260 At molecular level, tMCAo induced a significant downregulation of ciRS-7 in WT mice at 1dpi in
261 the peri-ischemic cortex, whereas the levels of miR-7-5p and Cyrano remained unaltered (Figure 4H,
262 Supplementary Figure S3C). However, ciRS-7 KO mice showed a significant upregulation of miR-
263 7-5p and unaltered levels of Cyrano (Figure 4H). These data suggest a correlation between the
264 absence of ciRS-7 and the upregulation of miR-7 in response to transient ischemic stroke.
265
266 ***ciRS-7 prevents miR-7 effects on glutamatergic signaling in excitatory neurons***
267 Previous studies have identified the involvement of miR-7 in response to oxidative stress[37], in
268 particular to low glucose[38]. To establish the possible functional link between the upregulation of miR-
269 7 in ciRS-7 KO mice in conditions of ischemic stroke, we subjected cre-loxP inducible miR-7 KO
270 mice[39] to tMCAo (Figure 5A, Supplementary Figure S4A,B). We failed to detect changes in the lesion
271 volume as measured by MRI between miR-7 KO and WT mice at acute timepoint (1dpi)
272 (Supplementary Figure S4C). In line with this data, miR-7 KO mice did not show any differences in
273 motor deficits compared to their WT controls (Supplementary Figure S4D). However, we detected
274 an increase in the lesion volume in miR-7 KO mice (Figure 5B) compared to their WT controls at
275 later timepoint (7 dpi), which was not associated with changes in Neuroscore (Supplementary Figure
276 S4E), suggesting a potential role of miR-7 in preventing the ischemia induced cell death.
277
278 To understand the functional role of miR-7 in ischemic stroke, we first validated that miR-7 has
279 functional target sites in our system through the analysis of miR-7 target binding sites using Ago2
280 HITS-CLIP sequencing data in pyramidal excitatory neurons[40] (Figure 5C). We identified RISC-
281 associated binding sites on expressed transcripts in mature projection neurons and the analysis of
282 minimal seed site hexamer of miR-7 revealed 645 potential targets in the 3′ UTRs (Figure 5D). As
283 expected, ciRS-7 obtained the highest number of functional binding sites (n=139) and accounted for

284 more than 11% of the total reads (Supplementary Table S7). The overlap between Ago2 HITS-CLIP
285 physical targets and the downregulated genes in the peri-ischemic cortex of ciRS-7 KO mice, where
286 miR-7 is upregulated, highlighted 276 common genes (Figure 5E). These genes were functionally
287 enriched in pathways related to glutamatergic synaptic transmission and morphological changes of
288 neuronal projections (Figure 5F, Supplementary Figure S5).
289 Given the central role of glutamatergic signaling in ischemia, these miR-7 potential targets in
290 excitatory neurons might relate the improved ischemic outcome and the increased levels of miR-7 in
291 ciRS-7 KO mice. To test this connection, we transduced ciRS-7 WT and KO neurons with lentivirus
292 overexpressing GFP and miR-7a or GFP only, under the neuronal specific human Synapsin 1 (hSyn)
293 promoter. Efficiency of infection was assessed through fluorescence microscopy (Supplementary
294 Figure S6A) and we validated with RT-qPCR that miR-7a-5p levels resembled the endogenous levels
295 in conditions of OGD (Supplementary Figure S6B).
296 Whilst overexpression of miR-7 in WT neurons did not affect the overall neuronal glutamate
297 excitability, increased levels of miR-7 in ciRS-7 KO neurons significantly reduced their response to
298 glutamate (Figure 5G), thus reverting the genotype of glutamate sensibility of the ciRS-7 KO neurons.
299 This appeared to be a glutamate specific effect, as the overexpression of miR-7 did not affect
300 GABAergic response (Supplementary Figure S6C).
301
302 Finally, to evaluate the functional impact of the potential targets of miR-7 involved in morphological
303 changes of neuronal projections (Figure 5F), we performed live imaging analysis of neurite outgrowth
304 of ciRS-7 KO and WT neurons infected with miR-7 lentivirus. In agreement with the calcium imaging
305 experiment, we were able to detect a significant increase in the neurite length when over expressing
306 miR-7 in ciRS-7 KO cells, but not in WT neurons (Figure 5H). This result is in line with a previous
307 study demonstrating a direct effect of miR-7 overexpression in controlling neurite length in a
308 neuroblastoma cell line[41]. However, circRNAs are known to be poorly expressed in cell lines due of

309 their high proliferation rate[42]. So, we wondered whether this miR-7 direct effect on neurite length
310 was due to lack of ciRS-7 interference. A study identifying circRNAs in neuronal cell lines and tissue
311 discovered that human neuroblastoma cell line expresses an exiguous amount of ciRS-7[42]. In addition,
312 we validated that murine neuroblastoma cell line N2A also express negligible levels of ciRS-7 even
313 when differentiated using retinoid acid, albeit the levels of Cyrano and miR-7 are more abundant
314 (Supplementary Figure S7A,B,C).
315
316
317 **DISCUSSION**
318
319 Here we identify how the ncRNAs network composed of ciRS-7 – miR-7 – Cyrano regulates cellular
320 responses to OGD *in vitro* and ischemic stroke *in vivo*. In OGD *in vitro* model, we identified a new
321 endogenous relationship between ciRS-7 and miR-7 than previously shown as ciRS-7 and Cyrano
322 downregulation occurred ahead of miR-7 upregulation which was not dependent on ciRS-7 presence.
323 In *in vivo* conditions, the absence of ciRS-7 alleviated cellular death and subsequent sensorimotor
324 deficits in response to ischemic stroke whereas the lack of miR-7 led to a more extensive tissue
325 damage. These effects were partially executed via regulation of glutamatergic signaling by miR-7.
326 Together these data highlight an endogenous regulatory role for the ciRS-7 network in mediating
327 cellular stress responses under pathophysiological conditions.
328
329 We hypothesize that our results on the ncRNAs network composed by ciRS-7, miR-7 and Cyrano
330 reflects a stress response mediated by miR-7 that is modulated by ciRS-7 and Cyrano expression. In
331 mouse, ciRS-7 harbors 130 MREs (binding sites) for miR-7[9] and, because of its extremely high
332 expression in neuron[5,9], the low levels of miR-7 in physiological conditions[5] are likely to be bound
333 to ciRS-7, as suggested by our pyramidal excitatory neurons CLIP-seq data and others[9,10]. Moreover,
334 Cyrano, which is also very abundant in neurons, harbors a single almost complementary site for miR-
335 7 which mediates miR-7 degradation[8]. Our data show that in physiological conditions strong and high

336 abundant miR-7 binding competitors (ciRS-7/Cyrano) interact with limited regulator (miR-7)
337 whereas in conditions of ischemic stroke, both *in vitro* and *in vivo*, there is a concomitant removal of
338 ciRS-7 and Cyrano and subsequent upregulation of miR-7. Our data showing a downregulation in
339 Cyrano prior to the upregulation of miR-7 is in line with previously known dynamics between these
340 two molecules as Cyrano triggers miR-7 degradation through TDMD[8]. On the other hand, here we
341 show for the first time the induction of miR-7 in the absence of ciRS-7 suggesting that expression
342 level of miR-7 is not dependent on ciRS-7 in conditions of ischemic stroke. This data, together with
343 the lack of involvement of miR-7 levels in ciRS-7 downregulation identified new endogenous
344 relationship induced by stress between miR-7 and ciRS-7 in respect of what it has been previously
345 shown in physiological conditions[8,9].
346
347 The role of miR-7 in ischemic stroke has been studied *in vivo* with controversial results[43,44]. Our large
348 cohort of animals revealed a high biological variability in expression levels of miR-7 in WT animals
349 subjected to transient ischemic stroke. This can be explained by the presence of feedback loops
350 between ciRS-7, Cyrano and miR-7 and suggests the idea that ciRS-7 and Cyrano may behave as a
351 buffer to regulate miR-7 expression. In line with this idea, ciRS-7 KO mice subjected to tMCAo
352 significantly overexpress miR-7 one day post-ischemia and show a reduced stroke lesion size and
353 motor deficits. Furthermore, at 7 dpi, miR-7 inducible KO mice showed an exaggerated ischemic
354 lesion size compared to WT animals, reinforcing the idea of a role of miR-7 in regulating ischemic
355 damage. Moreover, our data is in line with literature showing that the levels of miR-7 are
356 downregulated at early timepoints in ischemic stroke and that upregulation in miR-7 is necessary for
357 stroke recovery[45]. These data together propose a model in which ciRS-7 and Cyrano regulate miR-7
358 and possibly influence its upregulation acting as a “buffering” system.
359

360 Due to the lack of extensive changes in miR-7 targets in both ciRS-7, Cyrano and miR-7 KO animals
361 in physiological conditions[8,9], the exact role of ciRS-7 as an influencer of miR-7 target gene
362 expression has remained controversial. Our data show a significant shift in the overall expression of
363 miR-7 targets in conditions of OGD (Figure 2F), where a concerted downregulation of two strong
364 miR-7 regulators, ciRS-7 and Cyrano, occurs. Our data suggests that the inducible nature of this
365 network may explain the reported lack of extreme effects on miR-7 targets in physiological
366 conditions. This is supported by studies showing that single miRNA mutants exhibit a phenotype
367 solely under stress conditions[46,47]. Moreover, removal of a single competing target for endogenously
368 low expressed miRNAs, such as miR-7, is not expected to induce a relevant change in gene expression
369 in physiological conditions[15]. Finally, particularly for non-coding RNAs, cells are prone to adaptation
370 upon knock-out, generating an imbalance in output between knock-out and knock-down experiments,
371 as previously experienced[9].
372
373 We used the analysis of Ago2 CLIP-seq dataset to discover physiological interactions of miR-7 with
374 the downregulated genes in ciRS-7 KO tMCAo animals in which miR-7 is upregulated. Our data
375 suggest a role of miR-7 in regulating glutamatergic signaling and neuronal outgrowth. The central
376 role of glutamate in ischemic stroke pathophysiology is well established[12], contributing to the
377 neuronal loss upon exaggerated release and impaired clearance of glutamate in the synaptic cleft[11].
378 Overexpression of miR-7 failed to induce changes in glutamatergic signaling and neuronal outgrowth
379 in wild-type cortical neurons. However, in the absence of ciRS-7, miR-7 overexpression dampened
380 the neuronal glutamatergic response which likely contributes to the reduced cellular damage in
381 conditions of ischemic stroke.
382
383 Our hypothesis of ciRS-7 acting as a buffer on miR-7 mediated effects is strengthened further by our
384 data showing that miR-7 overexpression promotes neurite outgrowth only in ciRS-7 KO neurons,

385 which lack the ciRS-7 buffering effect. In line with our results, previously published data indicate
386 that miR-7 overexpression regulates neurite length in a neuroblastoma cell line[41]. Of note is that
387 murine neuroblastoma cell lines express negligible amounts of ciRS-7 even when differentiated with
388 retinoic acid, suggesting a more direct effect of miR-7 in the absence of its regulator. A recent study
389 has highlighted a potential role of miR-7 in controlling energy homeostasis in hypothalamic
390 neurons[39], linking this miRNA to conditions in which the energetic balance is strongly altered, such
391 as in ischemic stroke. However, alteration in the levels of miR-7 in hypothalamic neurons were not
392 accompanied by changes in the expression of ciRS-7 or Cyrano[39]. Together with our data showing
393 how the type of ischemic insult activates ciRS-7 network with different dynamics, this suggests that
394 the network responds in a stress type, strength, and duration dependent manner.
395
396
397 In summary, here we identify a role of ciRS-7 as a regulator of cellular stress response under OGD
398 *in vitro* and ischemic stroke *in vivo*. Upregulation of miR-7 following cerebral ischemia is critical for
399 the control of ischemic stroke induced damage and post-ischemia plasticity and depends on the levels
400 of ciRS-7. Our data support the role for ciRS-7 as a buffer of miR-7 effects against unwanted changes,
401 thus behaving as a "safe-guide" system. Finally, we propose a regulatory role for ciRS-7-miR-7
402 network in glutamatergic signaling through miR-7 target genes, hence providing a novel mechanism
403 which controls post-ischemia neuronal damage. More broadly, this study suggests a role of
404 intracellular network of non-coding RNAs in regulating pathophysiological processes in the brain.
405
406
407
408
409
410
411

412 # MATERIAL AND METHODS

413

414 **Primary cortical neuron culture preparation and OGD treatment**

415 Primary cortical neurons were prepared from C57BL/6J and C57BL/6N-Cdr1asem1Nikr (Cdr1as KO
416 and their WT counterpart) embryonic day 15 embryonal cortices. After dissection and removal of the
417 meninges, cortices were incubated 15 minutes at 37 °C in a solution of Krebs buffer (0.126 M NaCl,
418 2.5 mM KCl, 25 mM NaHCO3, 1.2 mM NaH2PO4, 1.2 mM MgCl2, 2.5 mM CaCl2, supplemented
419 with 45mM BSA, 0.8% of 3.85% MgSO4 and 1% Pen/Strep, pH 7.4) and 0.025% (w/v) trypsin
420 (Sigma-Aldrich, T 9201). Tissue was then treated with 0.008% w/v DNaseI (Sigma-Aldrich, DN25)
421 and 0.026% w/v trypsin inhibitor (Sigma-Aldrich, T9003) and centrifuged at 300 x g for 3 minutes.
422 Cell pellet was resuspended in 3ml of DNaseI/Trypsin solution and then diluted in 7ml of Krebs.
423 After centrifugation at 300 x g for 3 minutes the pellet containing embryonic neurons was
424 resuspended in cortical neurons growth media: Neurobasal (Gibco 21103049), B27 Supplement
425 (Gibco, 17504044), 0.2 mM L-glutamine (Lonza, BE17-605E), 0.01 mg/ml Penicillin/Streptomycin
426 (Gibco, 15140122). Cells were plated on Poly-D lysine (Sigma-Aldrich, P6407) freshly precoated
427 plates (50 µg/ml in sterile water plates for 1h at 37 °C and washed in sterile water prior use). Different
428 density was used for 6-well plates (1.8 million cells per well), 48-well plates (125.000 cells per well),
429 13mm plastic coverslips (30.000 cells per coverslip). After 5 days in culture half of the in cortical
430 neurons growth media was changed to fresh. Experiments were performed 7 days after the isolation
431 day. Cells were maintained in the incubator 37 °C, 5% CO2. For OGD treatment experiments, before
432 hypoxia induction the media was changed to Normoxic (cortical neurons growth media with
433 Neurobasal changed to Gibco A2477501 supplemented with D-Glucose 25mM and Sodium Pyruvate
434 0.2mM) or OGD (cortical neurons growth media with Neurobasal changed to Gibco A2477501).
435 Normoxic cells were then put back in the incubator, OGD cells were incubated in hypoxic chamber
436 37 °C, 5%CO_2, 1%O_2 (SCI-tive N, Ruskinn Technology). After the OGD timepoint cells were
437 harvested for RNA extraction or subjected to MTT colorimetric test.

438 **MTT test**

439 Cell viability was measured from 48-well plates treating the cells with (3-(4, 5-dimethylthiazolyl-2)-
440 2, 5-diphenyltetrazolium bromide), MTT reagent (Sigma-Aldrich, TOX1) diluted with culture media
441 at a final concentration of 120 µM. Triton-X 100 1% v/v (Sigma-Aldrich, X100) treated wells were
442 used as a positive control for this assay. Plates were incubated for 3-5h at +37°C. After, medium was
443 discarded, formazan crystals were dissolved with dimethyl sulfoxide (DMSO) (Sigma-Aldrich,
444 D2650) for 30min at RT in the dark. Absorbance was read at 585nm using Wallac 1420 Victor2
445 microplate reader (Perkin Elmer). Wells without cells were used as background and subtracted from
446 the absorbance data, all the six technical replicates were plotted for each of the three biological
447 replicate and the data was normalized on normoxic WT neurons or WT neurons infected with GFP
448 only.

449

450 **Neurite length measurement**

451 Neurons were seeded at a density of 125.000 cells/well in 48-well plates. After OGD exposure or
452 lentiviral infection, neurons were imaged at day 7 for 48 hours with IncuCyte® S3 Live Cell Analysis
453 System (Essen BioScience Ltd.) in bright field and green channel live cell images (two 10x
454 magnification images per well). Acquired data were analysed with the Incucyte® Neurotrack
455 Analysis Software Module (Sartorius) considering the average value of the two images taken for each
456 of the nine technical replicates for all the three biological replicates.

457

458 **RNA isolation and qRT-PCR**

459 Total RNA was extracted from primary cells and ipsilateral/contralateral animal cortex using
460 TRIzol™ Reagent (Invitrogen) following the manufacturer's instructions. 1µl of GlycoBlue™
461 Coprecipitant (Ambion) was added at the isopropanol step in each sample. RNA was quantified using
462 a Nanodrop 2000 spectrophotometer. 1 µg of total RNA was used for reverse-transcription

463 ofmRNAs, circRNA, lncRNAs and pri-miRNA species with High-Capacity cDNA Reverse
464 Transcription Kit (Applied Biosystems) following the manufacturer's protocol. SYBR Green qPCR
465 Master Mix (High ROX) (Bimake) and custom designed oligos were used to quantify mRNAs,
466 circRNAs, and lncRNAs following the manufacturer's indications. Mature microRNAs were reverse-
467 transcribed with TaqMan™ MicroRNA Reverse Transcription Kit (Invitrogen) using miRNA-
468 specific primers supplied in the TaqMan® probe kit for qPCR following the manufacturer's protocol.
469 Mature microRNAs and pri-microRNA PCRs were performed using Maxima Probe/ROX qPCR
470 Master Mix (Invitrogen) and TaqMan® specific probes (Thermofisher) following the manufacturer's
471 protocol. The result was analyzed with the ΔΔCT method and normalized geometric mean of 2
472 internal normalization controls (Gapdh and Rplp0) for SYBR green qPCRs and U6 expression for
473 TaqMan® miRNA and pri-miRNA. TaqMan® probes and sequence of the SYBR Green
474 oligonucleotide primers is available in the Supplementary Table S8.
475
476 **Lentivirus vectors and virus generation**
477 Lentiviral vectors LV1-eGFP (control) or LV1-eGFP-miR-7 were generated by subcloning inserts
478 from pAAV_hSYN1-eGFP-miR-7 and pAAV_hSYN1-eGFP (provided by Thomas B. Hansen)
479 inside LV1 (immunodeficiency virus 1 (HIV-1)-based LV-PGK-GFP) backbone by GenScript
480 Biotech Corporation. The generated construct contained HIV-1-LV backbone with hSYN1-eGFP-
481 miR-7 insert instead of PGK-GFPN inserted creating a terminal SmaI (CCCGGG) and a C-terminal
482 ApaI (GGGCCC) flanking restriction sites. The same was performed for the control vector with
483 hSYN1-eGFP insert only. 3rd generation lentiviral particles were produced by the BioCenter Kuopio
484 National Virus Vector Laboratory in Kuopio, Finland. The viral titer was assessed through qPCR
485 serial dilution quantification using eGFP ReadyMade™ Primers (IDT) (Supplementary Table S8).
486 Work with the virus vectors was carried out under permission from Finnish National Supervisory
487 Authority for Welfare and Health, Valvira. Cells were infected at day 2 post isolation with MOI 0.5

488 achieving 80% positive infected cells assessed by GFP expression in fluorescent microscope
489 (Supplementary Figure 5A) at day 7. The amount of overexpression of miR-7 was assessed by qPCR
490 as above specified (Supplementary Figure 5B).
491
492 **Library preparation**
493 All the samples RNA were isolated with TRIzol™ Reagent (Invitrogen) as specified above. RNA
494 samples were treated with TURBO DNA-free™ Kit (Ambion) following the manufacture's
495 instruction. RNA integrity was assessed through Agilent Bioanalyzer 2100 system with the Agilent
496 RNA 6000 Nano. The concentration of the samples was established with Qubit™ RNA Extended
497 range kit (Invitrogen). From cortical neurons subjected to OGD we generated 1) library to detect
498 circularRNAs and mRNA and lncRNAs using SMARTer® Stranded Total RNA Sample Prep Kit
499 (Takara Bio USA, Inc.) and 2) library for miRNAs detection utilizing NEBNext® Small RNA Library
500 Prep Set for Illumina (New England Biolabs (UK) Ltd) quality checked and size selected using pippin
501 prep method following manufacturer's protocol. We generated a library from ciRS-7 WT and KO
502 tMCAo animals contralateral and peri-ischemic cortices to detect mRNAs changes using CORALL
503 total RNA-Seq Library Prep Kit (Lexogen GmbH) after ribosomal RNA depletion of 600ng of RNA
504 with RiboCop rRNA Depletion Kit V1.2 (Lexogen GmbH). All the libraries were generated following
505 the manufacturer's protocol. After generation, the libraries were quantified with Qubit™ High
506 Sensitivity DNA kit (Invitrogen) and by qPCR using KAPA Library Quantification Kit for Illumina®
507 Platforms (Roche). Library size was determined with Agilent Bioanalyzer 2100 system using the
508 Agilent High Sensitivity DNA Kit. Cortical neurons samples to detect circularRNAs, mRNA, and
509 lncRNAs were sequenced paired-end 100 cycles on NovaSeq™ 6000 platform (Illumina) and single-
510 read 75 cycles on NextSeq™ 500 system (Illumina) to detect microRNAs. Animal samples were
511 sequenced single-read 75 cycles on NextSeq™ 550.
512

513 **Calcium imaging**

514 Calcium imaging was performed with murine E15 cortical neurons. The neurons were plated onto
515 PDL-coated circular plastic coverslips (13 mm diameter) in 12-well plate at a density of 30,000
516 cells/coverslip and kept for 5 days in Neurobasal medium supplemented with B27. To quantify and
517 compare the functional expression of glutamate and GABA receptors in neuronal cultures, we used
518 calcium-imaging technique as previously described[48]. Briefly, neuronal cultures were loaded with the
519 cell-permeable indicator Fluo-4am (Life Technologies, F10471) for 30 min at 37 °C, followed by 10
520 min washout, and placed in the perfusion chamber mounted on the stage of Olympus IX7010
521 microscope. Neurons were continuously perfused by basic salt solution (BSS) 3 ml/min containing
522 in mM: 152 NaCl, 10 HEPES, 10 glucose, 2.5 KCl, 2 CaCl2, 1 MgCl2 and pH adjusted to 7.4. Test
523 compounds diluted in the BSS to final concentrations were applied through fast perfusion system
524 (Rapid Solution Changer RSC-200, BioLogic Science Instruments). Cells were imaged with 10x
525 objective using Olympus IX-7010. Excitation wavelength was set as 494 nm, sampling frequency 2
526 FPS. Glutamate (100 µM with the co-agonist glycine 10 µM promoting activation of NMDA
527 receptors subtype) or GABA (100 µM) were applied for 2 s. Finally, KCl (50 mM) application for 2 s
528 was used to distinguish exciTable neurons from possible non-neuronal cells. Fluorescence was
529 detected with the Till Photonics imaging system (FEI GmbH) equipped with a 12-bit CCD Camera
530 (SensiCam) with a light excitation wavelength of 494 nm. Calcium responses to neurotransmitters
531 were evaluated from changes in fluorescence intensity of individual neurons. To this end, regions of
532 interest (ROI) of round shape around the cell body were selected from the whole image with the TILL
533 vision Imaging Software (TILL Photonics GmbH). To distinguish from non-neuronal cells, ROI was
534 taken at the time point corresponding to KCl-induced activation of neurons. The intensity values in
535 each ROI were averaged at each time point to form a fluorescence signal for each neuron and
536 normalized to the baseline level. Signals above 5% of the baseline were included in the analysis.

537

538 **N2a Cell culture**

539 Immortalized murine neuroblastoma cells (N2a) were maintained in DMEM, high glucose,
540 GlutaMAX™ Supplement (Gibco, 31966021) media supplemented with supplemented with 10%
541 Fetal Bovine Serum (Gibco, 10270106) and 1% penicillin and streptomycin in temperature controlled
542 humidified incubator (37 °C, 5%CO_2). As previously published[49], for differentiation induction
543 100.000 cells were plated in a 6-well plate and maintained in complete media supplemented with
544 20µM retinoic acid (Sigma-Aldrich, R2625) in dimethyl sulfoxide (DMSO) with or without serum
545 starvation (2% FBS instead of 10%) changing half of the media every second day for 5 days before
546 collection.

547

548 **MOUSE STRAINS AND ANIMAL PROCEDURES**

549 All experiments follow the Helsinki Declaration and guidelines set by the European Commission
550 (European Communities Council Directive, 86/609/EEC) and were approved by the National Animal
551 Experiment Board of Finland.

552 Animals were housed with same sex siblings, in controlled temperature, humidity and light (12 hours
553 light/dark cycle) conditions. Animals had access to ad libitum food. Before the beginning of the
554 animal study mice were divided in single cages. Mice were randomized and all the participants were
555 blinded to the genotype (surgery, MRI acquisition, behavioral test, sample collection and data
556 analysis). Prior to the surgery, we use random number generator (GraphPad Prism quick calcs
557 https://www.graphpad.com/quickcalcs/randomN1/) to randomize the mice into treatment groups.
558 This numbering has been used in crescent order on 3-4 months old male mice that were divided into
559 groups. pMCAo study was performed on 3-4 months old Balb/cOlaHsd male mice (n = 6-8 per
560 timepoint). Cdr1as (ciRS-7) KO tMCAo study was performed on 3-4 months old C57BL/6N-
561 Cdr1asem1Nikr[9] (Cdr1as KO mice and the WT counterpart), provided by Prof. Dr. Nikolaus
562 Rajewsky, MDC, Berlin, Germany (n = 22-24 per genotype). miR-7 inducible KO tMCAo study was

563 performed on 3-4 months old B6.Cg-miR7a1tm1(fl/fl)ms miR7a2tm1(fl/fl)ms miR7btm1(fl/fl)ms
564 Ndor1Tg(UBC-cre/ERT2)1Ejb/Stf and UBC-cre negative counterpart[39] provided by Prof. Dr.
565 Markus Stoffel, ETH, Zurich, Switzerland (n = 20-26 per genotype).
566
567 **Genotyping**
568 Before the animal studies, ciRS-7 KO and miR-7 KO mice were genotyped as before[9,39] except for
569 the tissue dissociation step. Briefly, ear puncture samples were digested in 50 mM Sodium Hydroxide
570 solution for one hour at 95 °C. Once equilibrated to room temperature the samples were neutralized
571 with 1M Tris Hydrochloride pH 8. Two microliters of digested samples were used to run the reaction
572 of PCR with Taq 2X Master Mix (New England Biolabs (UK) Ltd) following manufacturer protocol
573 and using the oligonucleotide primers as specified in Supplementary Table S8. The PCR products
574 were separated on a stained 2.5% or 1.5% Agarose gel for ciRS-7 and miR-7 KO respectively and
575 run in an electrophoresis chamber. Images were acquired with ChemiDoc Imaging Systems (Bio-Rad
576 Laboratories, Inc).
577
578 **Permanent middle cerebral artery surgery (pMCAo)**
579 Permanent middle cerebral artery occlusion (pMCAo) was performed in 3-4 months old
580 Balb/cOlaHsd male mice as previously described[50]. Briefly, mice were anesthetized using 5%
581 isoflurane and anesthesia was maintained with 2% isoflurane. Temperature of the animals was
582 controlled during the surgery with heating blanket and rectal probe (Harvard apparatus). After the
583 skin incision, the left temporal bone was exposed under the temporal muscle, and 1 mm hole was
584 drilled on top of bifurcation in the middle cerebral artery (MCA). The dura was gently removed, and
585 the MCA was lifted and permanently occluded under the bifurcation using a thermocoagulator (Aaron
586 Medical Industries Inc.). Success of the occlusion was confirmed by cutting the MCA above the
587 occlusion site. After the occlusion, the temporal muscle was replaced, and the wound was sutured.

588 The surgery was performed on a total of 20 mice, 3 mice (one per timepoint) died during the surgery
589 and was then not included.
590
591 **miR-7 KO induction with tamoxifen**
592 Before tMCAo surgery, miR-7 inducible KO mice were injected with 2mg of Tamoxifen
593 intraperitoneally once per day for 5 consecutive days at the age of 3 to 4 weeks as before[39].
594 Recombination was induced in both Cre+ and Cre- littermates. Tamoxifen (Sigma-Aldrich, T5648)
595 was resuspended in 90% corn oil (Sigma-Aldrich, C8267) and 10% pure ethanol and dissolved at
596 56°C for 30 minutes in the dark. After injection the mice were put on soft food diet and their weight
597 was monitored daily. Mice showing a successful genomic recombination in ear puncture samples two
598 weeks after injection were included in the study (Supplementary Figure S4A). At the end of the study
599 the animals were analyzed for miR-7 abrogation in the brain through RT-qPCR (Supplementary
600 Figure S4B).
601
602 **Transient middle cerebral artery surgery (tMCAo)**
603 Transient middle cerebral artery occlusion (tMCAo) was performed in 3-4 months old male Cdr1as
604 and miR-7 KO and WT mice as previously described[51]. Briefly, induction of anesthesia was
605 performed with 3.5-4% isoflurane in 0.5 L/min of 100% O2-enriched air and maintained at 1-1.5%
606 isoflurane during the surgery. The body temperature maintained at 36 ± 1°C during surgery with a
607 heating pad attached to a rectal probe. A Doppler probe was fixed on the temporal bone over the
608 MCA to monitor blood flow. The right common, external, and internal carotid arteries (CCA, ECA,
609 and ICA) were exposed through an incision in the neck. The arteries were carefully dissected, and a
610 6-0 silicon coated monofilament of 0.21 mm of diameter (Doccol Corporation) was inserted into the
611 right CCA or left ECA (Cdr1as and mir-7 KO respectively) and led through the ICA until blocking
612 the origin of the MCA. Blood flow blockage was monitored with the Doppler probe, and animals

613 with less than 80% of blood flow decrease were discarded. After one hour of occlusion, the
614 monofilament was withdrawn allowing blood reperfusion. Animals that did not show a correct
615 reperfusion measured by laser doppler were discarded from the study. Incisions were permanently
616 sutured, and the animals were allowed to recover in a temperature-controlled environment for 24
617 hours. The surgery was performed on a total of 32 WT and 25 Cdr1as KO mice, and 36 WT and 26
618 miR-7 KO. In the ciRS-7 animal study a total of 7 mice was excluded as: 2 KO and 2 WT mice lacked
619 reperfusion upon surgery, 2 WT and 1 KO mice died during the study. In the miR-7 animal study a
620 total of 12 mice was excluded as: 3 WT and 2 KO lacked reperfusion upon surgery, 4 WT and 3 KO
621 died during the study.
622
623 **Magnetic resonance imaging (MRI)**
624 MRI was performed at 1, 3, and 7dpi using a vertical 9.4 T/89 mm magnet (Oxford instrument
625 PLC) upon anesthesia with 1.8% isoflurane in 30% O2/70% N2O. We acquired twelve slices of
626 0.8mm thickness per mouse (echo time 40ms, repetition time of 3000ms, matrix size of 128 × 256
627 and field of view 19.2 × 19.2 mm^2) and analyzed the first seven images using the Aedes software
628 (http://aedes.uef.fi/) for MatLab program (Math-works). Upon definition of the region of interest
629 (ROI) of contralateral, ipsilateral, and lesion, the lesion volume normalized on oedema was
630 calculated on the first 7 section as: $Corrected\ lesion\ size\ =\ lesion\ size\ \times \left(1 -\right.$
631 $\left.\frac{[ipsilateral\ size - contralateral\ size]}{contralateral\ size}\right)$. The lesion size is expressed has percentage of lesion on the total
632 brain size.
633
634 **Neurological severity score (NSS)**
635 Mice were examined for neurological deficits at baseline and dpi 1, 3, and 7 using a severity scale
636 comprising the following tests: postural reflex, circling, falling to contralateral side, placement of the
637 contralateral forelimb during motion, and general state of alertness or consciousness. Deficits were

638 graded from 0 (normal) to 2 or 3 (severe)[52]. A sum of these scores were used for statistics. Behavioral
639 assessment was performed by an experimenter blinded to the genotype of mice.
640
641 **Transcardiac perfusion and sample collection**
642 After anesthesia, mice were perfused transcardially with cold saline solution with heparin 2500 IU/l
643 (Leo Pharma A/S). In the pMCAo study, the brains were collected and dissected into contralateral
644 and peri-ischemic cortical regions. In the tMCAo study the brains were cut in 6 coronal sections and
645 stained with 1% 2,3,5-Triphenyltetrazolium Chloride (TTC) (Sigma-Aldrich) in PBS solution for 5
646 minutes at 37 °C in agitation before dissection of contralateral and peri-ischemic cortical regions. For
647 immunohistochemistry staining, brains were collected and fixed in 4% paraformaldehyde solution in
648 0.1 M phosphate buffer (PB) pH 7.4. After 22 hours of fixation, the brains were transferred in 30%
649 sucrose in PB buffer solution for 48 hours and then frozen in liquid nitrogen before being stored in -
650 70 °C.
651
652 **GFAP immunostaining**
653 Each brain was then cut using a cryostat (Leica Microsystems) into six 20 µm coronal sections 400 µm
654 apart, collected on Superfrost™ Plus Microscope Slides (ThermoFisher Scientific) and stored in -
655 70°C until immunostaining. Sections were then rehydrated with phosphate-buffered saline (PBS) pH
656 7.4 for 10 min and PBS with 0.05% Tween-20 (PBST) (Sigma-Aldrich) for 5 min. Endogenous
657 peroxidase was blocked by using 0.3 % hydrogen peroxide (H_20_2) in MeOH for 30 min after which
658 sections were washed 3 x 5 min in PBST. Non-specific binding was blocked with 10 % normal goat
659 serum (NGS)(Vector, S-1000) in PBST for 1 h at RT Sections were incubated overnight at RT in
660 primary antibody rabbit anti-GFAP (Agilent, Dako Z0334,1:500 in 5 % NGS-PBST) and then with
661 biotinylated secondary antibody anti-rabbit IgG (H+L) (Vector, BA-1000, 1:200 in 5 % NGS-PBST)
662 for 2 h at RT followed by incubation in ABC reagent (Vector Elite Kit) for 2 h at RT. Sections were

663 washed 3 x 5 min in PBST before and after the incubations. Nickel-3,3'-diaminobenzidine (Ni-DAB)
664 solution (0.175M Sodium acetate, 1% Nickel ammonium sulphate, 50mg DAB (Sigma-Aldrich, D-
665 5905)) with 0.075 % H_20_2 was used to develop the colour for 6 min stopping the reaction by washing
666 the sections 2 x 5 min in dH_2O. Sections were then dehydrated in 50 % EtOH, 70 % EtOH, 95 %
667 EtOH, 100 % EtOH for 2 min in each and 3 x 5 min in xylene followed by mounting the coverslips
668 with Depex.
669
670 **Image acquisition & analysis**
671 Six GFAP immunoreactivity light microscope images per mouse were acquired by Leica DM6B-Z
672 Thunder Imager microscope (Leica Microsystems CMS GmbH) equipped with DMC2900 camera
673 using 10x magnification. Images were captured using LAS X software (Leica Microsystems CMS
674 GmbH) with exposure time 5 ms, color-gain mode: R:0-G:0-B:25. The images were quantified from
675 the peri-ischemic cortex next to the lesion border (1mm) and the corresponding area of the healthy
676 contralateral hemisphere from 10x images using ImageJ software[53] function "Measure particles". The
677 results were presented as relative immunoreactive area to the total area analyzed.
678
679 **RNA-seq data analysis**
680 Bulk RNA sequences of mRNA and miRNA have been aligned and quantified to the mouse genome
681 of reference mm10 with the Cdr1as annotation of "chrX:61183248|61186174|.|+" using the nf-core
682 workflow[54] (3.0 version of "rnaseq" and 1.1.0 version of "smrnaseq" applied without clipping and
683 the three prime adapter "AGATCGGAAGAGCACACGTCT"), while circular sequences using 1.1
684 CIRIquant[55] set to Read 1 matching the sense strand. Count data were prepared following the
685 workflow defined by Law et al[56]. We filtered out lowly expressed molecules in any condition using
686 the function "filterByExpr" to increase the reliability of the mean-variance relationship. We removed
687 the differences between samples due to the sequencing depth normalizing the count using the trimmed

688 mean of M-values (TMM)[57] method and applied a log transformation minimizing sum of sample-
689 specific squared difference to enhance the true positive and negative ratio in the downstream
690 analysis[58]. We checked for batch effect due to different timings in biological replicates preparation
691 by performing a principal component analysis and unsupervised consensus clustering with Cola[59].
692 We identified a batch effect due to different timings in biological replicates preparation influencing
693 the grouping of the normoxic and OGD samples in the dataset ciRS-7 KO/WT cortical neurons
694 (Supplementary Table S5). We corrected the batch effect of this dataset using the negative binomial
695 regression from Combat[60]. We adjusted the variance between the samples as before[61] through
696 winsorization[62]. We finally created the design matrix for each pair of conditions to compare (contrast)
697 and performed the differential expression analysis using limma/edgeR model[56] controlling for the
698 false discovery rate with Benjamini-Hochberg Procedure[63].
699

700 **Ingenuity Pathway Analysis (IPA) and Functional enrichment analysis**

701 We uploaded the differentially expressed genes of each contrast to QIAGEN IPA (QIAGEN Inc.,
702 https://digitalinsights.qiagen.com/IPA)[64] and Metascape[65] for Ingenuity pathway analysis and
703 functional enrichment analysis, respectively. The analysis has been performed with default
704 parameters and IPA's background was composed of non-differentially expressed genes.
705

706 **Deconvolution analysis with scRNAseq**

707 We exploited cell-type specific gene expression from external single-cell RNA sequencing (scRNA-
708 seq) data to define the cell subpopulations composing our cortical neuron culture (Supplementary
709 Table 2) and ischemic stroke animal tissue (Supplementary Table 6) bulk RNA sequencing datasets.
710 The scRNA-seq dataset of Loo et al.[66] of the mouse cerebral cortex at embryonic day 14.5 was
711 provided to SCDC[67] for performing the deconvolution of our gene expression matrix with cortical
712 neuron samples in normoxic conditions. The scRNA-seq data of Zeisel at al.[68] composed of murine

713 cerebral cortex samples from p25 to p60 was instead provided to MuSiC[69] to perform the
714 deconvolution of our gene expression matrix with contralateral and peri-ischemic samples of wild-
715 type and ciRS-7 KO ischemic stroke animals (Supplementary Table 6) as this method is designed to
716 work with multi-subject scRNA-seq dataset.
717
718 **GRO-seq data analysis**
719 A summary of all GRO-seq samples used to quantify pri-miRNA expression levels are presented in
720 Supplementary Table S3. Raw reads for public GRO-seq data were acquired from the GEO database.
721 GRO-Seq reads were trimmed using the HOMER v4.3 (http://homer.salk.edu/homer)[70] software to
722 remove A-stretches originating from the library preparation. From the resulting sequences, those
723 shorter than 25 bp were discarded. The quality of raw sequencing reads was controlled using the
724 FastQC tool (http://www.bioinformatics.babraham.ac.uk/projects/fastqc)[71] and bases with poor
725 quality scores were trimmed using the FastX toolkit (http://hannonlab.cshl.edu/fastx_toolkit/). Reads
726 were aligned to mouse mm9 reference genome using the Bowtie[72] version bowtie-0.12.7. Up to two
727 mismatches and up to three locations were accepted per read and the best alignment was reported.
728 The data was used to create Tag Directories using HOMER. To optimize coverage, a combined tag
729 directory representing all samples of a given cell type (under one or several GSE numbers) was
730 created and used for pri-miRNA quantification using the 'analyzeRepeats.pl' command and '-rpkm -
731 strand +' options". The dataset used in this analysis are reported in Supplementary Table S3.
732
733 **miRWalk analysis**
734 We associated the significantly deregulated miRNAs and differentially expressed genes of wild-type
735 and ciRS-7 KO cortical neurons subjected to OGD (Supplementary Table 2, Supplementary Table
736 4). We filtered miRNA-Target interactions obtained from 3.0 miRWalk[73,74] database with 99%
737 probability and located in the 3-UTR region and included Oip5os1 (Cyrano) as target of mmu-miR-

738 7a-5p[8]. We linked the differentially expressed miRNAs and genes of each contrast by anticorrelation
739 (e.g. miRNA with positive log fold change and significant adjusted probability value is associated to
740 genes with negative log fold change, significant adjusted probability value and targets in miRWalk
741 of the miRNA) focusing on mmu-miR-7a-5p.
742
743 **CDF generation**
744 We tested the assumption of anticorrelation between mmu-miR-7a-5p and its miRWalk gene targets
745 using the empirical Cumulative Distribution Function (eCDF). For each contrast, we compared the
746 eCDF (control function) obtained from the values of log fold change of the non-target genes against
747 the one of the miRNA's targets and tested their equality with the Kolmogorov–Smirnov test[75]. To
748 determine the magnitude and direction of the shift of the eCDF of the targets in respect of the non-
749 targets, we measured the area between the two curves following this formula: $\int \{F_Y(t) - F_X(t)\}\, dt$
750 and the Wasserstein distance[76]. Both the considered targets and non-targets genes passed the filtering
751 by expression, count normalization and participated at the differential expression analysis.
752
753
754 **CLIP-seq analysis**
755 We collected the HITS-CLIP dataset of Argonate 2 in pyramidal excitatory neurons produced by Tan
756 et al.[40] (Supplementary Table S9) and replicated the original analysis to map and annotate the
757 genomic regions with a significant read cluster (peak). Briefly, we performed a quality control with
758 FastQC (http://www.bioinformatics.babraham.ac.uk/projects/fastqc)[71] and applied trimming to
759 remove bases after 50 base pairs due to low quality. We applied Cutadapt[77] to remove adapters and
760 over-represented sequences. We selected reads of at least 24 nucleotides in length and quality score
761 higher than 20 for each nucleotide. Reads were aligned to the mouse reference genome mm10 using
762 Burrows-Wheeler aligner[78] with default parameters, then the mapped reads were expanded by 30

763 nucleotides on each side. We considered only reads present in at least 2 experimental replicates and
764 clusters composed of at least 10 overlapping reads. Bowtie[79] was used to map all occurrences of
765 sequences complementary to the 6mer seed sequence (positions 2-7 of the mature miRNA) of mouse
766 miRNAs from miRBase V21 (https://www.mirbase.org/) to the mouse genome mm10, allowing no
767 mismatches. Strand specific intersection was done with the filtered clusters in the 3'UTR, 5'UTR,
768 coding sequence (CDS) and intron regions from RefSeq gene definitions, as well as antisense matches
769 to RefSeq genes[80]. Strand specific intersection was also done to circRNAs from circBase[81]. This
770 generated a genome-wide list with predicted miRNA target sites backed by the detected Ago2 HITS-
771 CLIP clusters for all mouse miRNAs. A subset including all miR-7a-5p targets is supplied as
772 Supplementary Table S7. Only 3'UTR target sites were used to define miRNA mediated regulation.
773 The full list of all predicted miRNA target sites was uploaded to GEO, as described in the Data
774 Availability section.
775
776 **Statistical analysis**
777 Graphs and statistical analysis were performed in GraphPad Prism 9. Every Figure legend reports
778 parameters of replicates (n), statistical test and p-value obtained. Where not specified, p-value was
779 not statistically significant (p-value > 0.05). We refer to n in animal study as single biological
780 replicate (mouse) and in cortical neuron as technical replicates in the same batch, the experiment has
781 been performed in three independent biological replicates.
782
783 **Data availability**
784 The data produced and analyzed in this publication have been deposited in NCBI's Gene Expression
785 Omnibus[82] and are accessible through GEO Series accession number GSE213179, GSE213067,
786 GSE213177, GSE211552 and GSE215210 as presented in the Supplementary Table S9. The code

787 developed to analyze the data produced in this study is available upon request at
788 https://doi.org/10.5281/zenodo.7233809.
789

790 **ACKNOWLEDGEMENTS**

791 The authors acknowledge Nicholas Downes for the fruitful discussions, Mirka Tikkanen for her
792 technical assistance with immunohistochemistry staining, Reetta Vuolteenaho for mouse colony
793 maintenance and Miia Salo for assistance in the preparation of primary neuronal cultures. Moreover,
794 the authors acknowledge the Biocenter Kuopio National Virus Vector Laboratory technology service,
795 Cell and Tissue Imaging Unit of UEF, The Lab Animal Centre at the University of Eastern Finland
796 in particular Nina Liimatainen and Hanna Miettinen, for the support. The Biocenter Oulu Transgenic
797 and Tissue Phenotyping core facility, Oulu Laboratory Animal Centre Research Infrastructure,
798 Translational cell biology core facility at Kontinkangas campus and the Faculty of Biochemistry and
799 Molecular Medicine of the University of Oulu are also acknowledged. This project is co-founded by
800 Horizon 2020 Framework Programme of the European Union (Marie Skłodowska Curie grant
801 agreement No 740264). This study was supported by the Academy of Finland, The Finnish Cultural
802 Foundation, Finnish Foundation for Cardiovascular Research, Instrumentarium Science Foundation,
803 Inkeri and Mauri Vänskä Foundation, Saastamoinen Foundation and Kuopio University Foundation.
804 The illustrations present in this study were created with BioRender.com.
805

806 **AUTHOR CONTRIBUTIONS**

807 F.S. and T.M. conceived and planned the study; F.S., T.M., T.H., J.J., R. Giniatullin, and D.T.
808 provided intellectual contribution and contributed to the interpretation of the results; F.S., V.S., P.K.,
809 I.U., J.J, H.D., C.P., N.V and J. Koistinaho contributed to the *in vivo* experiments; F.S., V.S., D.M.T.,
810 M.G.B., R. Giniatullina, N.K., S.YH. contributed to the *in vitro* experiments; F.S., A. H.S., J.S., and
811 J. Kjems planned and performed the libraries for the RNA-seq experiments; L.G. planned and

812 generated the code for the bioinformatic analysis and analyzed RNA-seq data; M.L., M.P., M.S., N.R.
813 provided the transgenic animals and assisted in the animal study on these models; M.V. and A.S.
814 produced and analyzed the HITS-CLIP-seq data; R.H. coordinated and supported the sample
815 preparation in Oulu University by F.S., V.S., S.K. and A.H; M.K. analyzed the GRO-seq data; F.S.
816 and T.M. wrote the manuscript in consultation with T.H., J.J. R. Giniatullin, J. Kjems with input from
817 all authors. All authors provided critical feedback and helped shape the research, analysis and
818 manuscript.
819

820 **REFERENCES**

821 1. Mehler, M. F. & Mattick, J. S. Noncoding RNAs and RNA editing in brain development,
822 functional diversification, and neurological disease. *Physiol. Rev.* **87**, 799–823 (2007).
823 2. Lewis, B. P., Burge, C. B. & Bartel, D. P. Conserved seed pairing, often flanked by adenosines,
824 indicates that thousands of human genes are microRNA targets. *Cell* **120**, 15–20 (2005).
825 3. Mattick, J. S. & Makunin, I. V. Small regulatory RNAs in mammals. *Hum. Mol. Genet.* **14 Spec**
826 **No 1**, R121-132 (2005).
827 4. Fatica, A. & Bozzoni, I. Long non-coding RNAs: new players in cell differentiation and
828 development. *Nat. Rev. Genet.* **15**, 7–21 (2014).
829 5. Hansen, T. B. *et al.* Natural RNA circles function as efficient microRNA sponges. *Nature* **495**,
830 384–388 (2013).
831 6. Kristensen, L. S. *et al.* The biogenesis, biology and characterization of circular RNAs. *Nat. Rev.*
832 *Genet.* **20**, 675–691 (2019).
833 7. Hansen, T. B. *et al.* miRNA-dependent gene silencing involving Ago2-mediated cleavage of a
834 circular antisense RNA: miRNA mediated cleavage of circular antisense RNA. *EMBO J.* **30**,
835 4414–4422 (2011).

836 8. Kleaveland, B., Shi, C. Y., Stefano, J. & Bartel, D. P. A Network of Noncoding Regulatory
837 RNAs Acts in the Mammalian Brain. *Cell* **174**, 350-362.e17 (2018).
838 9. Piwecka, M. *et al.* Loss of a mammalian circular RNA locus causes miRNA deregulation and
839 affects brain function. *Science* **357**, eaam8526 (2017).
840 10. Memczak, S. *et al.* Circular RNAs are a large class of animal RNAs with regulatory potency.
841 *Nature* **495**, 333–338 (2013).
842 11. Olney, J. W., Rhee, V. & Ho, O. L. Kainic acid: a powerful neurotoxic analogue of glutamate.
843 *Brain Res.* **77**, 507–512 (1974).
844 12. Dirnagl, U., Iadecola, C. & Moskowitz, M. A. Pathobiology of ischaemic stroke: an integrated
845 view. *Trends Neurosci.* **22**, 391–397 (1999).
846 13. Tiedt, S. & Dichgans, M. Role of Non-Coding RNAs in Stroke. *Stroke* **49**, 3098–3106 (2018).
847 14. Leung, A. K. L. & Sharp, P. A. MicroRNA Functions in Stress Responses. *Mol. Cell* **40**, 205–
848 215 (2010).
849 15. Denzler, R. *et al.* Impact of MicroRNA Levels, Target-Site Complementarity, and
850 Cooperativity on Competing Endogenous RNA-Regulated Gene Expression. *Mol. Cell* **64**, 565–
851 579 (2016).
852 16. Salmena, L., Poliseno, L., Tay, Y., Kats, L. & Pandolfi, P. P. A ceRNA hypothesis: the Rosetta
853 Stone of a hidden RNA language? *Cell* **146**, 353–358 (2011).
854 17. Franco-Zorrilla, J. M. *et al.* Target mimicry provides a new mechanism for regulation of
855 microRNA activity. *Nat. Genet.* **39**, 1033–1037 (2007).
856 18. Zhang, Y. *et al.* Circular RNAs in the Regulation of Oxidative Stress. *Front. Pharmacol.* **12**,
857 (2021).
858 19. Loo, L. *et al.* Single-cell transcriptomic analysis of mouse neocortical development. *Nat.*
859 *Commun.* **10**, 134 (2019).

860 20. Semenza, G. L. Hypoxia-inducible factor 1: control of oxygen homeostasis in health and
861 disease. *Pediatr. Res.* **49**, 614–617 (2001).
862 21. Zhang, J., Chen, S., Yang, J. & Zhao, F. Accurate quantification of circular RNAs identifies
863 extensive circular isoform switching events. *Nat. Commun.* **11**, 90 (2020).
864 22. Loppi, S. *et al.* Peripheral inflammation preceeding ischemia impairs neuronal survival through
865 mechanisms involving miR-127 in aged animals. *Aging Cell* **20**, e13287 (2021).
866 23. Step, S. E. *et al.* Anti-diabetic rosiglitazone remodels the adipocyte transcriptome by
867 redistributing transcription to PPARγ-driven enhancers. *Genes Dev.* **28**, 1018–1028 (2014).
868 24. Meng, F.-L. *et al.* Convergent transcription at intragenic super-enhancers targets AID-initiated
869 genomic instability. *Cell* **159**, 1538–1548 (2014).
870 25. Min, I. M. *et al.* Regulating RNA polymerase pausing and transcription elongation in
871 embryonic stem cells. *Genes Dev.* **25**, 742 (2011).
872 26. Fang, B. *et al.* Circadian enhancers coordinate multiple phases of rhythmic gene transcription in
873 vivo. *Cell* **159**, 1140–1152 (2014).
874 27. Hah, N. *et al.* Inflammation-sensitive super enhancers form domains of coordinately regulated
875 enhancer RNAs. *Proc. Natl. Acad. Sci.* **112**, E297–E302 (2015).
876 28. Heinz, S. *et al.* Effect of natural genetic variation on enhancer selection and function. *Nature*
877 **503**, 487–492 (2013).
878 29. Escoubet-Lozach, L. *et al.* Mechanisms Establishing TLR4-Responsive Activation States of
879 Inflammatory Response Genes. *PLOS Genet.* **7**, e1002401 (2011).
880 30. Ji, Z. *et al.* Transcriptional activity regulates alternative cleavage and polyadenylation. *Mol.*
881 *Syst. Biol.* **7**, 534 (2011).
882 31. Zhang, F. *et al.* Enhancer-bound LDB1 regulates a corticotrope promoter-pausing repression
883 program. *Proc. Natl. Acad. Sci.* **112**, 1380–1385 (2015).

884 32. Telese, F. *et al.* LRP8-Reelin-regulated Neuronal (LRN) Enhancer Signature Underlying
885 Learning and Memory Formation. *Neuron* **86**, 696–710 (2015).
886 33. Sticht, C., Torre, C. D. L., Parveen, A. & Gretz, N. miRWalk: An online resource for prediction
887 of microRNA binding sites. *PLOS ONE* **13**, e0206239 (2018).
888 34. Dweep, H. & Gretz, N. miRWalk2.0: a comprehensive atlas of microRNA-target interactions.
889 *Nat. Methods* **12**, 697–697 (2015).
890 35. Zeisel, A. *et al.* Molecular Architecture of the Mouse Nervous System. *Cell* **174**, 999-1014.e22
891 (2018).
892 36. Yoon, J. S. *et al.* Spatiotemporal Protein Atlas of Cell Death-Related Molecules in the Rat
893 MCAO Stroke Model. *Exp. Neurobiol.* **27**, 287–298 (2018).
894 37. Kabaria, S. *et al.* MicroRNA-7 activates Nrf2 pathway by targeting Keap1 expression. *Free*
895 *Radic. Biol. Med.* **89**, 548–556 (2015).
896 38. Chaudhuri, A. D., Kabaria, S., Choi, D. C., Mouradian, M. M. & Junn, E. MicroRNA-7
897 Promotes Glycolysis to Protect against 1-Methyl-4-phenylpyridinium-induced Cell Death. *J.*
898 *Biol. Chem.* **290**, 12425–12434 (2015).
899 39. LaPierre, M. P., Lawler, K., Godbersen, S., Farooqi, I. S. & Stoffel, M. MicroRNA-7 regulates
900 melanocortin circuits involved in mammalian energy homeostasis. *Nat. Commun.* **13**, 5733
901 (2022).
902 40. Tan, C. L. *et al.* MicroRNA-128 Governs Neuronal Excitability and Motor Behavior in Mice.
903 *Science* **342**, 1254–1258 (2013).
904 41. Chen, H. *et al.* miR-7 and miR-214 are specifically expressed during neuroblastoma
905 differentiation, cortical development and embryonic stem cells differentiation, and control
906 neurite outgrowth in vitro. *Biochem. Biophys. Res. Commun.* **394**, 921–927 (2010).
907 42. Rybak-Wolf, A. *et al.* Circular RNAs in the Mammalian Brain Are Highly Abundant,
908 Conserved, and Dynamically Expressed. *Mol. Cell* **58**, 870–885 (2015).

909 43. Yao, G.-Y. *et al.* Ischemic postconditioning confers cerebroprotection by stabilizing VDACs
910 after brain ischemia. *Cell Death Dis.* **9**, 1–15 (2018).
911 44. Zhao, J. & Wang, B. MiR-7-5p Enhances Cerebral Ischemia-Reperfusion Injury by Degrading
912 sirt1 mRNA. *J. Cardiovasc. Pharmacol.* **76**, 227–236 (2020).
913 45. Mehta, S. L. *et al.* CDR1as regulates α-synuclein-mediated ischemic brain damage by
914 controlling miR-7 availability. *Mol. Ther. Nucleic Acids* **31**, 57–67 (2023).
915 46. Bushati, N. & Cohen, S. M. microRNA functions. *Annu. Rev. Cell Dev. Biol.* **23**, 175–205
916 (2007).
917 47. Miska, E. A. *et al.* Most Caenorhabditis elegans microRNAs are individually not essential for
918 development or viability. *PLoS Genet.* **3**, e215 (2007).
919 48. Tiihonen, J. *et al.* Sex-specific transcriptional and proteomic signatures in schizophrenia. *Nat.*
920 *Commun.* **10**, 3933 (2019).
921 49. Kumar, M. & Katyal, A. Data on retinoic acid and reduced serum concentration induced
922 differentiation of Neuro-2a neuroblastoma cells. *Data Brief* **21**, 2435–2440 (2018).
923 50. Korhonen, P. *et al.* Immunomodulation by interleukin-33 is protective in stroke through
924 modulation of inflammation. *Brain. Behav. Immun.* **49**, 322–336 (2015).
925 51. Shahjouei, S. *et al.* Middle Cerebral Artery Occlusion Model of Stroke in Rodents: A Step-by-
926 Step Approach. *J. Vasc. Interv. Neurol.* **8**, 1–8 (2016).
927 52. Senda, D. M., Franzin, S., Mori, M. A., de Oliveira, R. M. W. & Milani, H. Acute, post-
928 ischemic sensorimotor deficits correlate positively with infarct size but fail to predict its
929 occurrence and magnitude after middle cerebral artery occlusion in rats. *Behav. Brain Res.* **216**,
930 29–35 (2011).
931 53. Schneider, C. A., Rasband, W. S. & Eliceiri, K. W. NIH Image to ImageJ: 25 years of image
932 analysis. *Nat. Methods* **9**, 671–675 (2012).

933 54. Ewels, P. A. *et al.* The nf-core framework for community-curated bioinformatics pipelines. *Nat.*
934 *Biotechnol.* **38**, 276–278 (2020).
935 55. Zhang, J., Chen, S., Yang, J. & Zhao, F. Accurate quantification of circular RNAs identifies
936 extensive circular isoform switching events. *Nat. Commun.* **11**, 90 (2020).
937 56. Law, C. W. *et al.* RNA-seq analysis is easy as 1-2-3 with limma, Glimma and edgeR.
938 *F1000Research* **5**, (2016).
939 57. Robinson, M. D. & Oshlack, A. A scaling normalization method for differential expression
940 analysis of RNA-seq data. *Genome Biol.* **11**, R25 (2010).
941 58. Zhang, Z. *et al.* Novel Data Transformations for RNA-seq Differential Expression Analysis.
942 *Sci. Rep.* **9**, 4820 (2019).
943 59. Gu, Z., Schlesner, M. & Hübschmann, D. cola: an R/Bioconductor package for consensus
944 partitioning through a general framework. *Nucleic Acids Res.* **49**, e15 (2021).
945 60. Zhang, Y., Parmigiani, G. & Johnson, W. E. ComBat-seq: batch effect adjustment for RNA-seq
946 count data. *NAR Genomics Bioinforma.* **2**, lqaa078 (2020).
947 61. Allswede, D. M. *et al.* Complement Gene Expression Correlates with Superior Frontal Cortical
948 Thickness in Humans. *Neuropsychopharmacology* **43**, 525–533 (2018).
949 62. Winsor, C. P., Hastings, C., Mosteller, F. & Tukey, J. W. Low Moments for Small Samples: A
950 Comparative Study of Order Statistics. *Ann. Math. Stat.* (1947) doi:10.1214/aoms/1177730388.
951 63. Benjamini, Y. & Hochberg, Y. Controlling the False Discovery Rate: A Practical and Powerful
952 Approach to Multiple Testing. *J. R. Stat. Soc. Ser. B Methodol.* **57**, 289–300 (1995).
953 64. Krämer, A., Green, J., Pollard, J. & Tugendreich, S. Causal analysis approaches in Ingenuity
954 Pathway Analysis. *Bioinforma. Oxf. Engl.* **30**, 523–530 (2014).
955 65. Zhou, Y. *et al.* Metascape provides a biologist-oriented resource for the analysis of systems-
956 level datasets. *Nat. Commun.* **10**, 1523 (2019).

957 66. Loo, L. *et al.* Single-cell transcriptomic analysis of mouse neocortical development. *Nat.*
958 *Commun.* **10**, 134 (2019).
959 67. Dong, M. *et al.* SCDC: bulk gene expression deconvolution by multiple single-cell RNA
960 sequencing references. *Brief. Bioinform.* **22**, 416–427 (2021).
961 68. Zeisel, A. *et al.* Molecular Architecture of the Mouse Nervous System. *Cell* **174**, 999-1014.e22
962 (2018).
963 69. Wang, X., Park, J., Susztak, K., Zhang, N. R. & Li, M. Bulk tissue cell type deconvolution with
964 multi-subject single-cell expression reference. *Nat. Commun.* **10**, 380 (2019).
965 70. Heinz, S. *et al.* Simple combinations of lineage-determining transcription factors prime cis-
966 regulatory elements required for macrophage and B cell identities. *Mol. Cell* **38**, 576–589
967 (2010).
968 71. Blankenberg, D. *et al.* Manipulation of FASTQ data with Galaxy. *Bioinformatics* **26**, 1783
969 (2010).
970 72. Langmead, B., Trapnell, C., Pop, M. & Salzberg, S. L. Ultrafast and memory-efficient
971 alignment of short DNA sequences to the human genome. *Genome Biol.* **10**, R25 (2009).
972 73. Dweep, H. & Gretz, N. miRWalk2.0: a comprehensive atlas of microRNA-target interactions.
973 *Nat. Methods* **12**, 697–697 (2015).
974 74. Sticht, C., Torre, C. D. L., Parveen, A. & Gretz, N. miRWalk: An online resource for prediction
975 of microRNA binding sites. *PLOS ONE* **13**, e0206239 (2018).
976 75. Smirnov, N. Table for Estimating the Goodness of Fit of Empirical Distributions. *Ann. Math.*
977 *Stat.* **19**, 279–281 (1948).
978 76. Kantorovich, L. V. Mathematical Methods of Organizing and Planning Production. *Manag. Sci.*
979 **6**, 366–422 (1960).
980 77. Martin, M. Cutadapt removes adapter sequences from high-throughput sequencing reads.
981 *EMBnet.journal* **17**, 10–12 (2011).

78. Li, H. & Durbin, R. Fast and accurate short read alignment with Burrows–Wheeler transform. *Bioinformatics* **25**, 1754–1760 (2009).

79. Trapnell, C., Pachter, L. & Salzberg, S. L. TopHat: discovering splice junctions with RNA-Seq. *Bioinforma. Oxf. Engl.* **25**, 1105–1111 (2009).

80. Kd, P., T, T. & Dr, M. NCBI Reference Sequence (RefSeq): a curated non-redundant sequence database of genomes, transcripts and proteins. *Nucleic Acids Res.* **33**, (2005).

81. Glažar, P., Papavasileiou, P. & Rajewsky, N. circBase: a database for circular RNAs. *RNA N. Y. N* **20**, 1666–1670 (2014).

82. Edgar, R., Domrachev, M. & Lash, A. E. Gene Expression Omnibus: NCBI gene expression and hybridization array data repository. *Nucleic Acids Res.* **30**, 207–210 (2002).

FIGURES

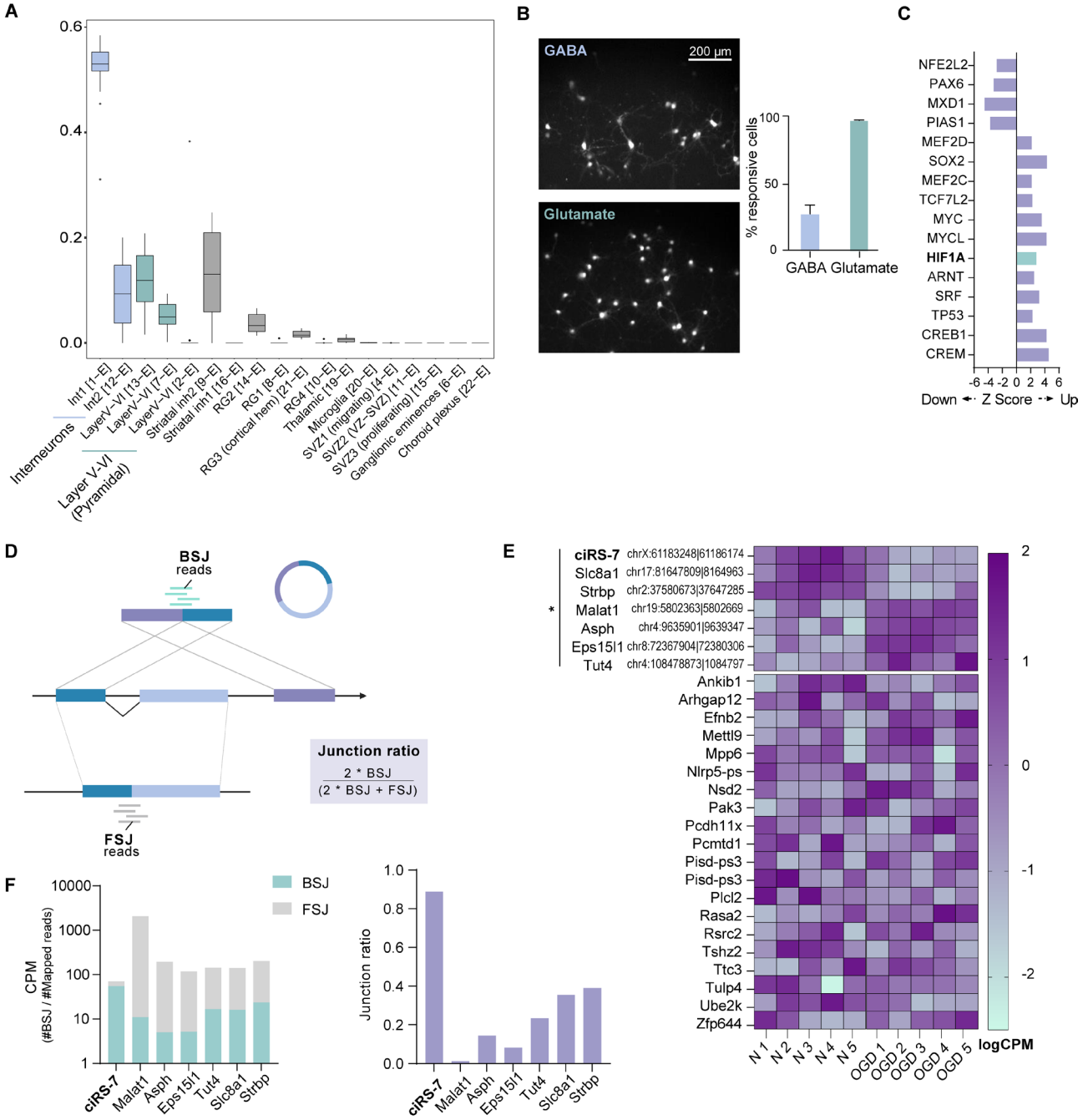

Figure 1. ciRS-7 is the most abundant circRNA in mouse cortical neuron cultures and downregulated by in vitro OGD.

(A) Box plot of bulk RNA-seq deconvolution scores. Cell types are sorted based on the median of the universal semantic groups which belong to (e.g. Int1, Int2 in Interneurons). **(B)** Calcium imaging analysis of the cellular response to glutamate and GABA with representative fluorescence images (n = 11 biological replicates; signal included > 5% of baseline; data as mean ± SD). **(C)** Bar plot of

1027 Ingenuity pathway analysis (IPA) conducted on bulk RNA-seq data of cortical neurons treated with
1028 OGD. Z-score indicates IPA prediction of transcription factor activation (positive value) or inhibition
1029 (negative value). Green color highlights HIF1α activation (|z|> 2 is considered significant). **(D)**
1030 Schematic representation of CIRIquant algorithm. Gene composed by three exons (dark blue, light
1031 blue, purple) generating a circular molecule through back-splicing or a linear transcript. In green
1032 specific circular reads on the back-splice junction (BSJ), in gray reads generated from forward
1033 splicing junctions (FSJ) in the same back-splicing region. Junction ratio score formula calculates a
1034 circularization score, higher the score and higher percentage of circular form of the gene of interest.
1035 **(E)** Heat map of logCPM of detected circularRNAs between normoxic (N) and oxygen and glucose
1036 deprived (OGD) murine cortical neuron culture. Blue color represents low expression and purple
1037 color represents high expression. Significant differentially expressed circularRNA grouped with a bar
1038 (* = adj. p-value < 0.05, n = 5 biological replicates). **(F)** (*left*) bar plot of CPM of the BSJ and FSJ of
1039 differentially expressed circularRNAs between normoxic and oxygen and glucose deprivation
1040 conditions, BSJ represents circular specific reads. (*right*) bar plot of the Junction ratio score calculated
1041 by CIRIquant algorithm. The score is a ratio of BSJ reads and FSJ reads mapped to BSJ site and
1042 represents percentage of circularization in respect of the linear transcript.

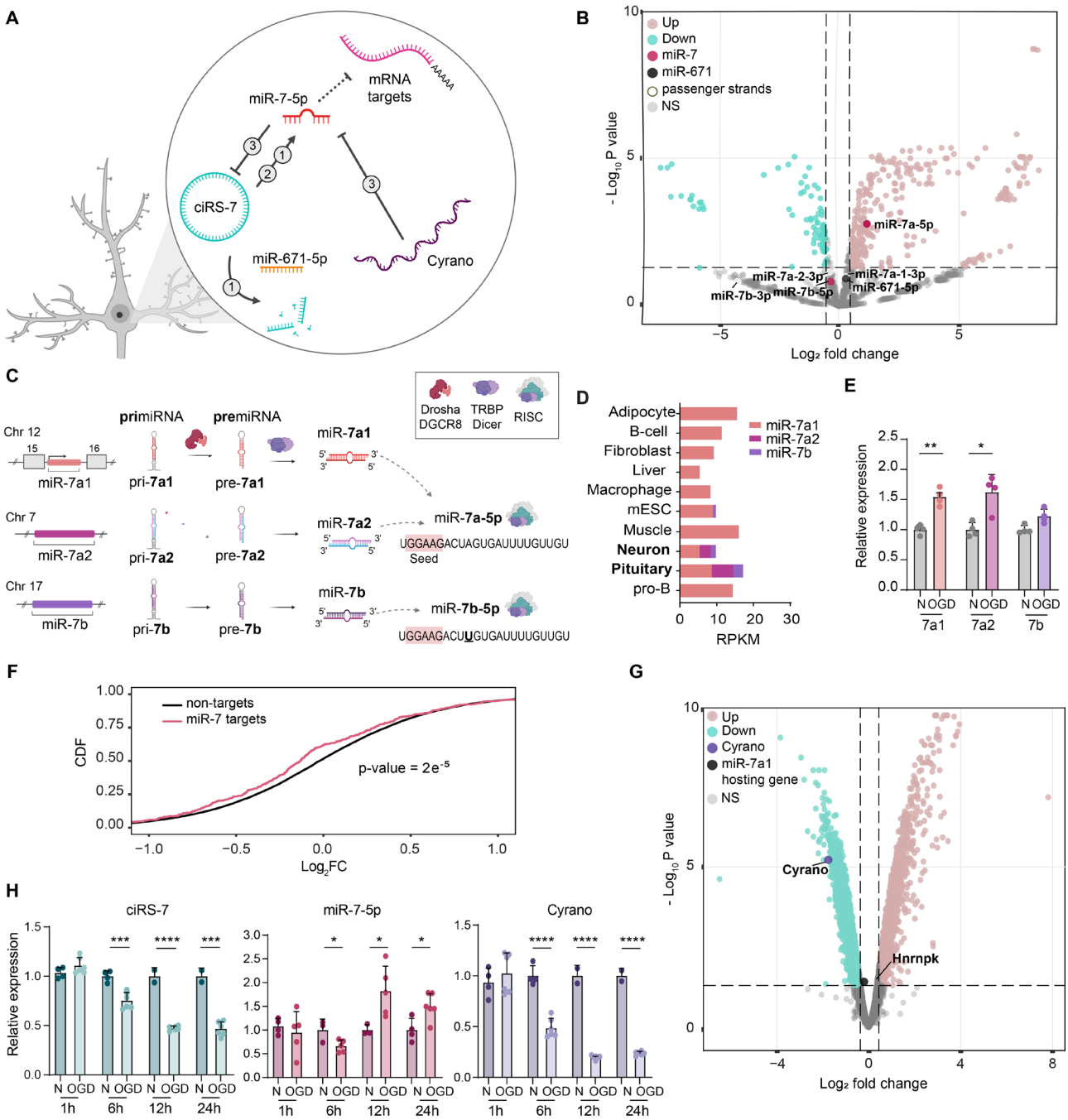

Figure 2. ciRS-7 network is dynamically altered in ischemic stroke like conditions.

(A) Schematic illustration of the relationships between the molecules of the regulatory network composed by ciRS-7, miR-7, Cyrano and miR-671. (1) Hansen et al. EMBO J, 2011; Hansen et al. Nature, 2013; (2) Piwecka et al. Science, 2017; (3) Kleaveland et al. Cell, 2018. **(B)** Volcano plot of differentially expressed microRNAs in cortical neuron cultures treated with OGD. Highlighted significantly upregulated (pink) and downregulated (green) microRNAs, miR-7 variants (red), miR-7 passenger strands (white), miR-671 (black) (n = 5 biological replicates; p-adj. <0.05 and |log2FC|> 0.3). **(C)** Schematic illustration of the murine genomic loci from which miR-7 primary transcripts

(pri-miR) are transcribed, processed in precursor molecules (pre-miR) and finally into mature miR-7. Highlighted in red the seed sequence shared between miR-7a-5p and miR-7b-5p, underlined in black the non-seed mismatch in position 10 between the variants. **(D)** Bar plot of reads per kilobase million (RPKM) of miR-7 genomic loci in different cell type obtained from GRO-seq datasets. **(E)** Bar plot of the expression of miR-7 pri-mirna in cortical neuron after OGD treatment quantified by quantitative PCR. Relative expression normalized on normoxic condition (n = 4; * = p-value < 0.05, ** = p-value < 0.01 calculated with paired t-test; data as mean ± SD). **(F)** Plot of the cumulative distribution functions (CDFs) of the log fold changes of genes compared between OGD treated wild-type cortical neurons for 12h and normoxic conditions. Red curve is the CDF obtained with only miR-7 targets, while black curve with non-targets (n = 5 biological replicates; p-value calculated with Kolmogorov-Smirnov test). **(G)** Volcano plot of differentially expressed transcripts in cortical neuron cultures treated with OGD. Highlighted significantly upregulated (pink) and downregulated (green) transcripts, Cyrano (purple), miR-7 hosting gene HnrnpK (black) (n = 5 biological replicates; p-adj. <0.05 and |log2FC|> 0.3). **(H)** Bar plot of the quantification by quantitative PCR of ciRS-7 (blue), miR-7 (magenta), Cyrano (purple) in cortical neurons OGD treated at different timepoints (1 hour, 6 hours, 12 hours and 24 hours). Relative expression normalized on normoxic condition (normoxia n = 2-4, OGD n=5-6; * = p-value < 0.05, *** = p-value < 0.001, **** = p-value < 0.0001 calculated with unpaired t-test; data as mean ± SD).

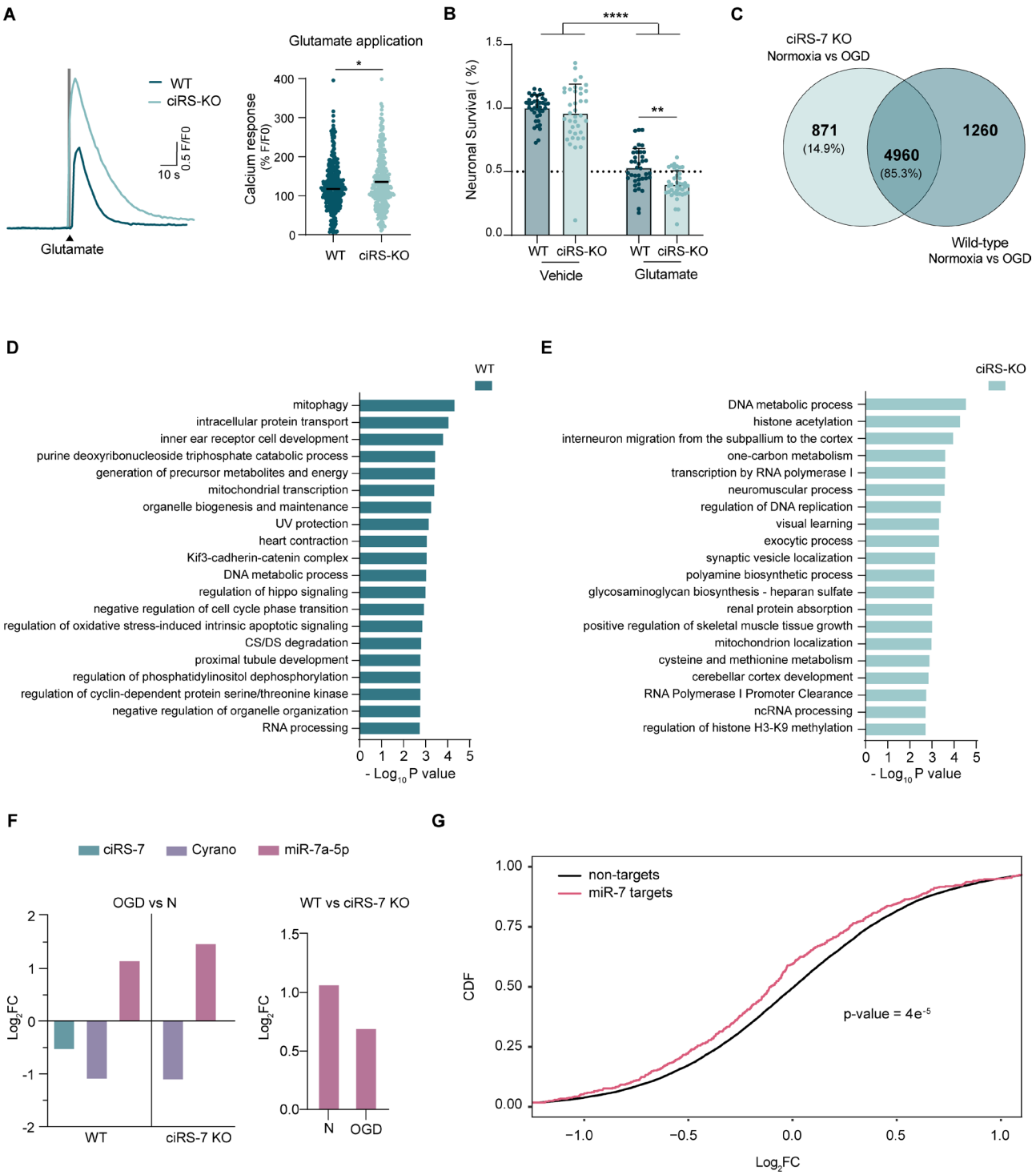

Figure 3. ciRS-7 knock-out genotype exhibit differential OGD response without affecting the OGD induced changes in miR-7 and Cyrano.

(A) (*left*) Representative trace of calcium induced fluorescence in response to glutamate treatment in wild-type and ciRS-7 KO cortical neurons. (*right*) Scatter dot plot of calcium imaging analysis of the cellular response to glutamate of wild-type and ciRS-7 KO cortical neurons. (n = 8 biological replicates; signal included > 5% of baseline; * = p-value < 0.05 calculated with unpaired t-test; central

1089 bar represents median value). **(B)** Bar plot of relative absorbance in MTT viability assay of wild-type
1090 and ciRS-7 KO cortical neurons treated with vehicle or glutamate 250μM. Data expressed as survival
1091 % normalized on wild-type vehicle (n = 4 biological replicates; * = p-value < 0.05, **** = p-value <
1092 0.0001 calculated with one-way ANOVA corrected with Tukey's post-hoc test; data as mean ± SD).
1093 **(C)** Venn diagram of the differentially expressed genes in normoxic versus OGD condition of wild-
1094 type and ciRS-7 KO cortical neurons (n = 5 biological replicates; p-adj. <0.05 and |log2FC|> 0.3).
1095 **(D)** Bar plot of functional enrichment analysis top 20 significant Metascape clusters performed on
1096 differentially expressed genes in wild-type normoxic versus OGD cortical neurons. **(E)** Bar plot of
1097 functional enrichment analysis top 20 significant Metascape clusters performed on differentially
1098 expressed genes in ciRS-7 KO normoxic versus OGD cortical neurons. **(F)** (*left*) Bar plot of log2FC
1099 of ciRS-7 (blue), miR-7 (magenta) and Cyrano (purple) obtained from RNA-seq of wild-type and
1100 ciRS-7 KO cortical neurons in normoxic conditions versus OGD. (*right*) Bar plot of log2FC of miR-
1101 7 (magenta) obtained from RNA-seq showing differences in the expression in normoxic conditions
1102 (N) or OGD between the wild-type and ciRS-7 KO genotype (n = 5 biological replicates; p-adj. <0.05
1103 and |log2FC|> 0.3). **(G)** Plot of the cumulative distribution functions (CDFs) of the log fold changes
1104 of genes compared between OGD treated ciRS-7 KO cortical neurons for 12h and normoxic
1105 conditions. Red curve is the CDF obtained with only miR-7 targets, while black curve with non-
1106 targets (n = 5 biological replicates; p-value calculated with Kolmogorov-Smirnov test).
1107

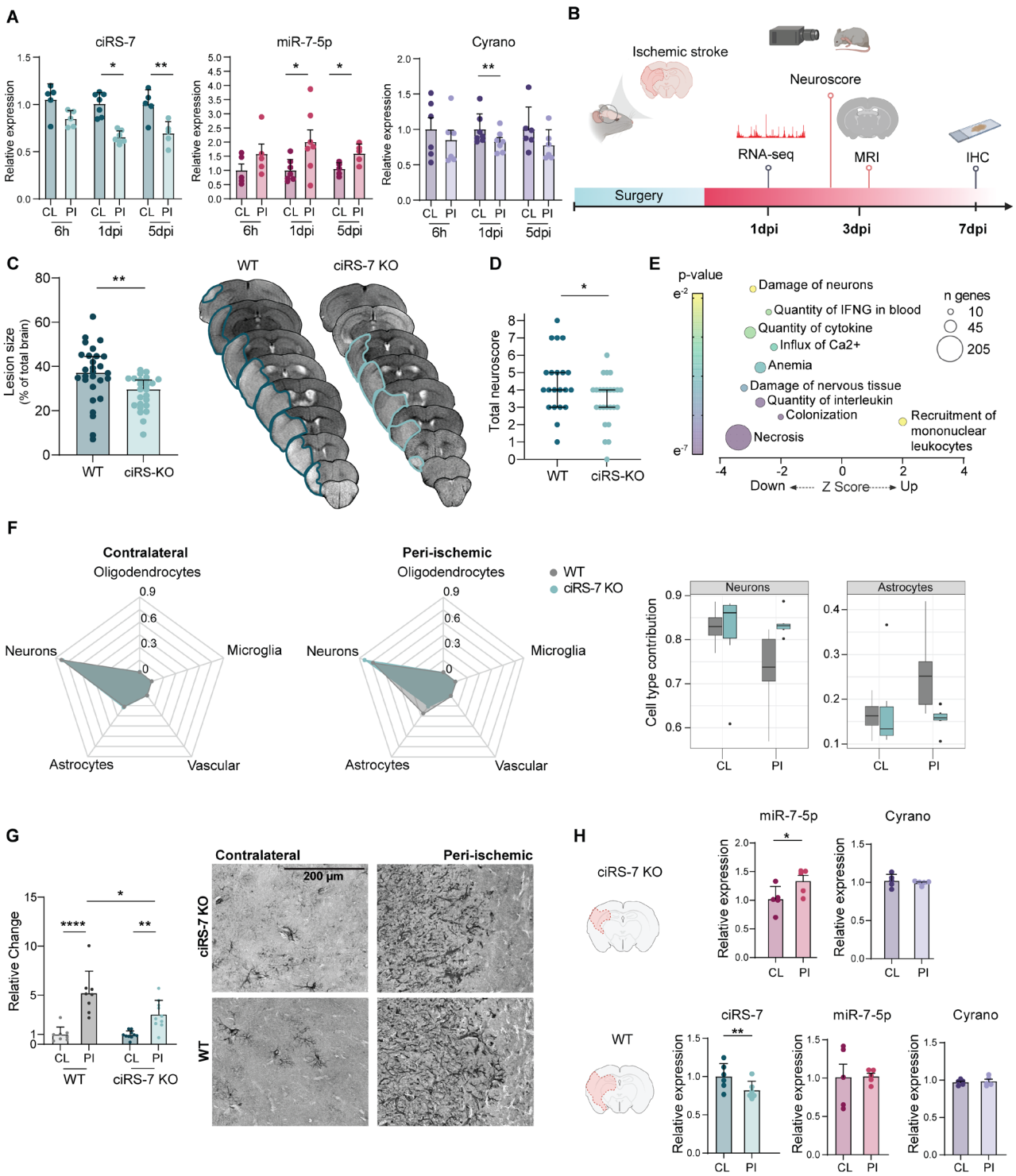

Figure 4. Lack of ciRS-7 ameliorates ischemic stroke outcome in vivo.

(A) Bar plot of the quantification by quantitative PCR of ciRS-7 (blue), miR-7 (magenta), Cyrano (purple) in 3-4 months old BALB/c mice subjected to pMCAo surgery. Peri-ischemic (PI) and contralateral (CL) cortices were collected at different timepoints (6 hours, 1 day and 5 days). Relative expression normalized on the average expression of CL (n = 6-7; * = p-value < 0.05, *** = p-value < 0.001, **** = p-value < 0.0001 calculated with paired t-test; data as mean ± SD). **(B)** Schematic illustration of the experimental design: wild-type and ciRS-7 KO mice were subjected to tMCAo

1116 surgery and monitored with neuroscore testing and MRI at 1 day, 3 days and 7 days post-surgery
1117 (dpi). Six mice were used at 1dpi to obtain peri-ischemic and contralateral cortices to perform RNA-
1118 sequencing. Eight to nine mice per group were used at dpi post ischemia for immunohistochemistry
1119 analysis. **(C)** (*left*) Bar plot of MRI quantification of the lesion size of wild-type and ciRS-7 KO mice
1120 subjected of tMCAo 1 day post-surgery. Data expressed as lesion percentage on total brain size
1121 adjusted for oedema (n = 25-28 per group; ** = p-value < 0.01 calculated with Mann–Whitney test;
1122 data as median with 95% confidence interval). (*right*) Representative image of lesion perimeter (blue)
1123 changes measured by MRI between wild-type (WT) and ciRS-7 KO animals. **(D)** Scatter dot plot of
1124 sensorimotor deficits measured by neuroscore in tMCAo wild-type and ciRS-7 KO mice at 1dpi (data
1125 expressed as total neuroscore; n = 22-25 per group; * = p-value < 0.05 calculated with Mann–Whitney
1126 test; data as median with 95% confidence interval). **(E)** Bubble plot of Ingenuity Pathway Analysis
1127 of differentially expressed genes between wild-type and ciRS-7 KO peri-ischemic cortices obtained
1128 through RNA-seq. Z-score indicates IPA prediction of pathway activation (positive value) or
1129 inhibition (negative value) in ciRS-7 KO. Color bar expresses p-value significancy (yellow to purple),
1130 size expresses the number of genes contained in the pathway (|z|> 2 is considered significant, pathway
1131 containing >10 genes were included). **(F)** (*left*) Spiderweb plot of wild-type (gray) and ciRS-7 KO
1132 (blue) contralateral and peri-ischemic cortices bulk RNA-seq deconvolution scores. (*right*) Bar plot
1133 of neurons and astrocyte contribution based on deconvolution scores in wild-type (gray) and ciRS-7
1134 KO (blue) contralateral and peri-ischemic regions. **(G)** (*left*) Bar plot of quantification of GFAP DAB
1135 (3,3′-Diaminobenzidine) immunostaining of wild-type and ciRS-7 KO tMCAo mice at 7dpi. (*right*)
1136 representative images of the staining highlighting GFAP+ cells. Relative expression normalized on
1137 the average expression of contralateral of wild-type mice (n = 8; * = p-value < 0.05, ** = p-value <
1138 0.01, **** = p-value < 0.0001 calculated with one-way ANOVA corrected with Tukey's post-hoc
1139 test; data as mean ± SD). **(H)** Bar plot of the quantification by quantitative PCR of ciRS-7 (blue),
1140 miR-7 (magenta), Cyrano (purple) in contralateral (CL) and peri-ischemic (PI) cortices of ischemic
1141 wild-type and ciRS-7 KO mice at 1dpi. Schematic representation correlating it to MRI lesion size at
1142 the same timepoint. Data are normalized on the average expression of contralateral of wild-type mice
1143 (n = 5 per group; * = p-value < 0.05, ** = p-value < 0.01 calculated with paired t-test; data as mean
1144 ± SD).
1145

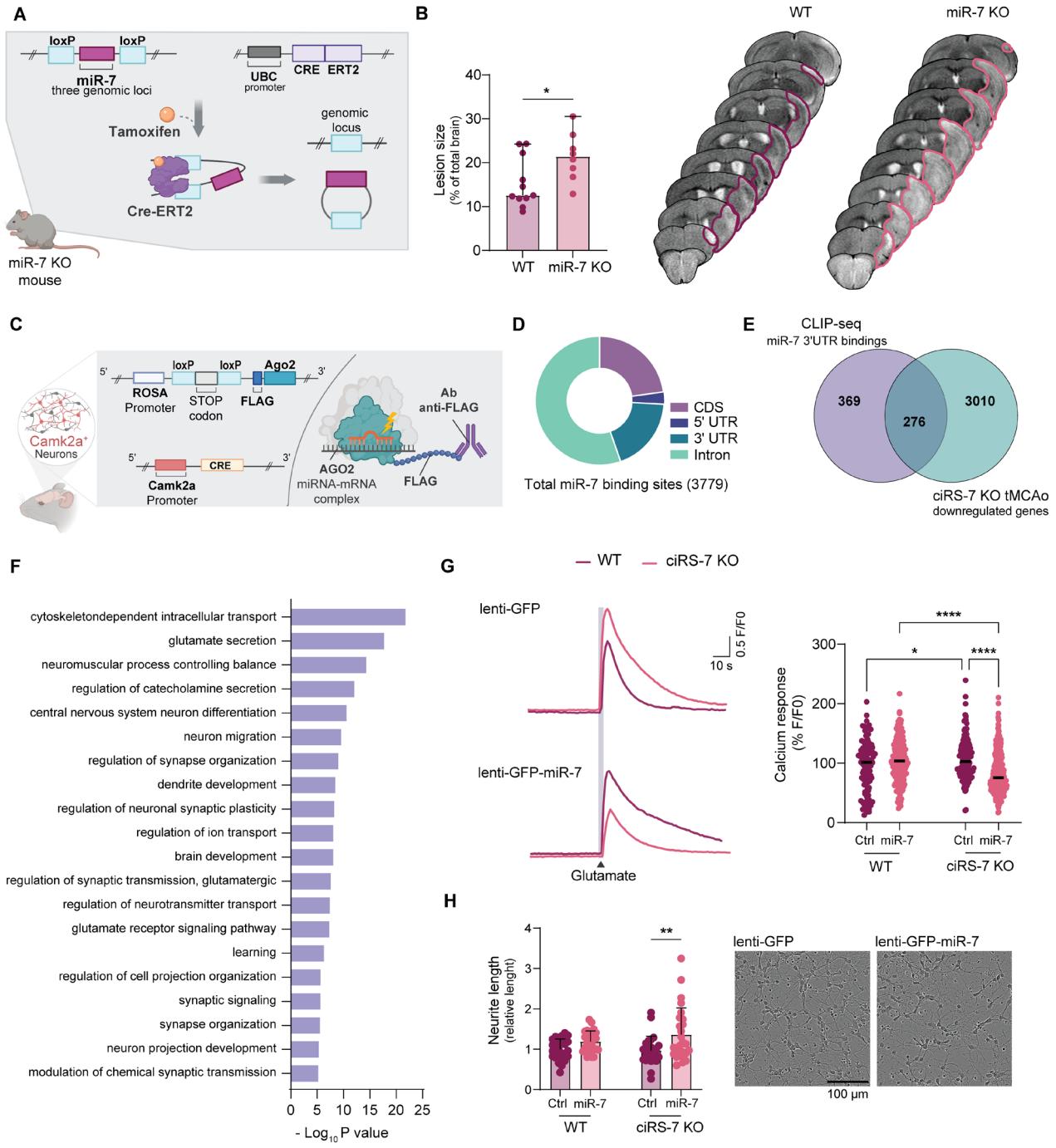

Figure 5. Lack of miR-7 exaggerates ischemic stroke outcome regulating glutamatergic response.

(A) Schematic illustration of Cre-LoxP miR-7 KO animal model. Mice transgenic genome with LoxP sequences (blue) flanking all the three miR-7 loci (magenta) and tamoxifen (orange) inducible Cre recombinase (purple). Tamoxifen activation of the Cre recombinase results in miR-7 loci deletion. Control mice are not transgenic for Cre recombinase. **(B)** (*left*) Bar plot of MRI quantification of the lesion size of wild-type and miR-7 KO mice subjected of tMCAo one day post-surgery. Data expressed as lesion percentage on total brain size adjusted for oedema (n = 8-11 per group; * = p-

value < 0.05 calculated with Mann–Whitney test; data as median with 95% confidence interval). (*right*) Representative image of lesion perimeter (blue) changes measured by MRI between wild-type (WT) and miR-7 KO animals. **(C)** Schematic illustration of recombinant mice utilized in to generate Ago2 CLIP-seq data in excitatory neurons. FLAG-Ago2 (blue) is translated only in Cam2Ka+ (red) excitatory neurons in which Cre recombinase (yellow) expression lead to FLAG-Ago2 translation due to the removal of a stop codon (gray). After cross-linking (thunder) FLAG-Ago2-miRNA-target complex is immunoprecipitated with anti-FLAG antibody (purple) and the miRNA-target complex output is sequenced. **(D)** Pie chart of the distribution of miR-7 binding sites obtained by CLIP-seq analysis. The 3779 identified binding sites are divided into protein coding sequences (CDS, purple), 5' untranslated regions (5' UTR, blue), 3' untranslated regions (3' UTR, dark green), intronic sequences (Intron, light green). **(E)** Venn diagram of the miR-7 binding sites in the 3' UTR identified by CLIP-seq in excitatory neurons (645) and the downregulated genes in ciRS-7 KO tMCAo animals peri-ischemic region (3286), in which miR-7 is upregulated. The genes resulting from the overlap of these datasets (276) represent miR-7 physical targets potentially affected in ischemic stroke. **(F)** Bar plot of functional enrichment analysis top 20 significant Metascape clusters performed of the genes identified as miR-7 physical targets potentially affected in ischemic stroke. **(G)** (*left*) Representative trace of calcium induced fluorescence in response to glutamate treatment in wild-type and ciRS-7 KO neurons infected with miR-7 or control lentivirus. (*right*) Scatter dot plot of the calcium imaging analysis quantifying the cellular response to glutamate of wild-type and ciRS-7 KO cortical neurons infected with control (GFP) or miR-7 overexpressing (GFP + miR-7) virus (n = 5 biological replicates; signal included > 5% of baseline; * = p-value < 0.05, **** = p-value < 0.0001 calculated with Kruskal–Wallis test; central bar represent median value). **(H)** (*left*) Bar plot of neurite length quantified through live imaging of wild-type type and ciRS-7 KO cortical neurons infected with control (GFP) or miR-7 overexpressing lentivirus (GFP + miR-7). Data normalized on average neurite length of wild-type GFP infected neurons (n = 3 biological replicates, n = 8 technical replicates; ** = p-value < 0.01 calculated with one-way ANOVA test corrected with Tukey's post-hoc test; data as mean ± SD). (*right*) Representative image of ciRS-7 KO cortical neurons infected with control (GFP) or miR-7 overexpressing virus (GFP + miR-7).